American Mineralogist, Volume 78, pages 511–532, 1993

# A transmission and analytical electron microscope study of exsolution microstructures and mechanisms in the orthoamphiboles anthophyllite and gedrite

EUGENE A. SMELIK,* DAVID R. VEBLEN
Department of Earth and Planetary Sciences, The Johns Hopkins University, Baltimore, Maryland 21218, U.S.A.

## ABSTRACT

An investigation of exsolution microstructures in 17 orthoamphibole samples (anthophyllite and gedrite) has been carried out using transmission and analytical electron microscopy (TEM and AEM). All the amphiboles studied, even those appearing to be optically homogeneous, contain exsolution lamellae. TEM observations show a wide variety of exsolution microstructures, ranging from extremely coarse lamellae over 200 nm in thickness to very fine scale, homogeneously distributed Guinier Preston (GP) zones. Many samples show evidence of progressive exsolution during slow cooling of the samples.

Evidence for heterogeneous nucleation and growth of lamellae is abundant, with (100) stacking faults and (010) chain-width errors (CWEs) as common nucleation sites. Heterogeneous nucleation has also been observed at grain boundaries, dislocations, and microfractures and along the interfaces of oxide inclusions. TEM images suggest that the incoherent terminations of (010) CWEs and (100) stacking faults are regions of significant structural distortion and lattice strain. These areas of high local strain energy appear to be responsible for unusual lamellar morphologies consisting of embayments in the lamellae caused by boundary pinning of the lamellar interfaces. In addition, there is considerable bulging of lamellae in the vicinity of (010) CWE terminations, which may result from enhanced chemical diffusion along the structural tunnels associated with the defect terminations, as well as from strain effects. In many samples, heterogeneous nucleation and growth was followed by homogeneous nucleation of smaller platelets in the solute-depleted regions between the larger lamellae.

The most common lamellar orientation was found to be (010). Other lamellar orientations have also been observed, including curved lamellae straddling (010), (140), (130), and (120). Calculations using the three-dimensional lattice fitting program, EPLAG, for intergrown anthophyllite and gedrite indicate that the combination of $\Delta b$ and $\Delta a$ between the amphiboles controls the actual lamellar orientations. If $\Delta b$ dominates over $\Delta a$, then a (010) optimal phase boundary is predicted. As $\Delta b$ decreases and $\Delta a$ increases, the optimal phase boundary gradually shifts from (010) to (120). AEM of the observed (120) exsolution microstructures suggests that increased Ca content is largely responsible for this orientation. The differences in lattice parameters are also sensitive to the Na content and Fe/Mg ratio.

AEM analyses of exsolved pairs of anthophyllite and gedrite indicate that edenite and tschermakite substitutions are of central importance in controlling exsolution. The exsolved pairs define the widest gap found to date for coexisting orthoamphiboles. Plotting the AEM data on the $T$-$X$ solvus diagrams of Spear (1980) suggests that exsolution typically took place between 460 and 520 °C.

## INTRODUCTION

Exsolution phenomena providing evidence of immiscibility between the orthoamphiboles anthophyllite and gedrite were first observed in the early part of the 20th century (Bøggild, 1905, 1924). Since that time, there have been numerous studies of coarse-grained coexisting anthophyllite and gedrite, which have led to a rather complete delineation of the miscibility gap between these amphiboles (e.g., Robinson and Jaffe, 1969a; Robinson et al., 1969, 1970, 1971a; Stout, 1970, 1971, 1972; Spear, 1980; Crowley and Spear, 1981; Stoddard and Miller, 1990). These studies primarily made use of optical petrography and electron microprobe (EMP) analysis to identify and determine compositions of coexisting amphiboles on either side of the solvus. Exsolution microstructures between anthophyllite and gedrite have also been studied extensively. Optical microscopy only allows

* Present address: Department of Geological and Geophysical Sciences, Princeton University, Princeton, New Jersey 08544, U.S.A.

0003–004X/93/0506–0511$02.00

observation of very coarse exsolution lamellae, which usually form parallel to (010) (e.g., Robinson et al., 1969; Spear, 1980; Stoddard and Miller, 1990), whereas XRD techniques permit recognition of submicroscopic exsolution lamellae through splitting of the (0*k*0) reflections (e.g., Robinson et al., 1969; Ross et al., 1969; Hawthorne et al., 1980; Wolter and Seifert, 1984). Transmission electron microscopy (TEM) has also been used to examine the structural details of fine-scale exsolution in anthophyllite and gedrite (Christie and Olsen, 1974; Gittos et al., 1976; Treloar and Putnis, 1982). These TEM studies have been important in demonstrating a high degree of complexity with respect to exsolution among orthoamphiboles, revealing complicated lamellar morphologies, new lamellar orientations, and structural defects that may be important during the unmixing process. The previous TEM studies, unfortunately, did not provide detailed compositional information for the exsolved phases, because of the lack of adequate analytical technology. Gittos et al. (1976), however, did present some early analytical electron microscopy (AEM) data using the EMMA-4 microscope, which did not allow for measurement of Na content.

The present study represents an in-depth TEM and AEM exploration of exsolution phenomena in the orthoamphibole system. Seventeen samples of anthophyllite and gedrite from several localities have been examined with the following goals in mind: (1) determination of the scale and distribution of exsolution microstructures as a function of amphibole composition, (2) determination of the exsolution history and exsolution mechanisms operating during unmixing, (3) identification of structural defects and their role during exsolution, (4) understanding the factors controlling the two previously recognized lamellar orientations, (010) and (120), and comparing all observed orientations with those predicted by optimal phase boundary theory, (5) comparison of AEM results from exsolved samples with previously reported EMP and AEM data on similar pairs of anthophyllite and gedrite.

## Experimental technique

All the orthoamphibole samples described below were first examined with the petrographic microscope. Many of the samples contain optically visible exsolution lamellae. In other samples, the amphiboles appear homogeneous, with no evidence of exsolution. Samples for TEM and AEM study were prepared by ion milling selected areas of petrographic thin sections. Electron microscopy was performed with a Philips EM420 transmission electron microscope operated at 120 keV and equipped with a SuperTwin (ST) objective lens (spherical aberration coefficient $C_s$ = 1.2 mm, chromatic aberration coefficient $C_c$ = 1.2 mm). For high-resolution (HRTEM) imaging, the objective aperture diameter either matched the point resolution of the microscope (0.30 nm) or was smaller.

Energy-dispersive X-ray spectra were obtained with an EDAX SiLi detector and processed with a Princeton Gamma-Tech model 4000 analyzer, as described by Livi and Veblen (1987). All amphibole analyses were recalculated to a 23-O basis following the method of Robinson et al. (1982), assuming all Fe to be $Fe^{2+}$. It should also be mentioned that AEM analyses are of inherently poorer quality compared with electron microprobe analyses, especially for Na, because of Na loss in the beam and low detection efficiency. Furthermore, additional analytical errors are usually introduced when analyzing very small precipitates, because the overall count rates are much lower than for larger areas (see discussion of AEM procedures in Appendix 2 of Livi and Veblen, 1987, for more information).

## Sample description

Seventeen orthoamphibole samples from six geographic localities have been examined in this study. Many of these sample localities contain multiple amphibole assemblages consisting of combinations of anthophyllite, gedrite, hornblende, and cummingtonite. Detailed analyses of these multiple amphibole assemblages have been given in earlier studies (see references below).

Five samples are from the Post Pond and Ammonoosuc Volcanics in east-central Vermont, collected from areas studied in detail by Spear (1977, 1978, 1980, 1982) and Spear and Rumble (1986a). Detailed descriptions of the outcrop locations (showing even the poison ivy locations), including mineral assemblages, given by Spear and Rumble (1986b, p. 284–288), and personal field maps kindly provided by Frank Spear greatly aided in the collection of these samples.

Seven orthoamphibole samples are from a locality known as Amphibole Hill in the Ammonoosuc Volcanics in southwestern New Hampshire and have been studied in detail by Robinson and coworkers (Robinson and Jaffe, 1969a, 1969b; Ross et al., 1969; Robinson et al., 1970, 1971a; Schumacher and Robinson, 1986, 1987; Schumacher, 1988). Six of these samples were kindly provided by John Schumacher, and one was collected by E.A.S.

One sample of gedrite was collected from coarse-grained gedrite-rich amphibolites from near Surry Mountain, New Hampshire. The rock came from an outcrop in the Ashuelot River about 300 m east of the junction of N.H. Rte. 12A and Gilsum Rd.

Two samples of gedrite were obtained from nearly monomineralic gedrite layers within marbles and pelitic schists of the Cherry Creek metamorphic section of the Gravelly range in southwestern Montana and were kindly provided by Jerry Murphy. The geology of this area has been described by Heinrich and Rabbitt (1960).

Two samples of orthoamphibole from metamorphic rocks in Colorado were also obtained. One, donated by Dusty Earley, is a sample of cordierite-gedrite gneiss that occurs as lenses within metabasalts near Ohio City, Colorado, as described by Earley and Stout (1991). The other is a sample of very coarse gedrite gneiss, collected by E.A.S., from the Front range, near Morrison, Colorado.

**TABLE 1.** Characteristics of orthoamphiboles used in this study

| Sample, this study | Sample, in literature and references[A] | Amphiboles present[B] | Optically visible exsolution lamellae | Other optical features[C] | *P-T*[D] conditions | Associated minerals[E] |
|---|---|---|---|---|---|---|
| | | **Amphibole Hill** | | | | |
| | | | | | 625–650 °C | |
| 7A0BX | 7A0BX[1,2,3] | gedrite | none | 2 | ~6 kbar | qt, bi, st, chl, gar, ky, sil |
| 7A7H2 | 7A7H2[3] | gedrite | none | 2 | | qt, pl, bi, op, rut |
| 7A7L | 7A7L[3] | anthophyllite, hornblende | none | 2 | | bi, gar, chl, cor, pl |
| 7A7J | 7A7J[3] | gedrite | none | 2 | | pl, cor, op |
| W95 | W95JX[1,4,5,6]; W95SX[7]; W95JXS[7] | gedrite | always | none | | cor, bi, rut, ky, sil, st |
| 6A9S | 6A9X[1,4,6,8]; 6A9S[3] | anthophyllite, gedrite, hornblende, cummingtonite | ortho: sometimes; hbld: ($\bar{1}$01), (100) | 2 | | pl, bi |
| 89-2 | 6A9X[1,4,6,8]; 6A9S[3] | anthophyllite, gedrite, hornblende, cummingtonite | ortho: sometimes; hbld: ($\bar{1}$01), (100) | 2 | | pl, bi |
| | | **Post Pond area**[F] | | | | |
| | | | | | 530 ± 25 °C ~4–6 kbar | |
| 89-18B | 77-56C[9,10]; 77-57[10]; 77-58D[10] | anthophyllite, gedrite, cummingtonite | ortho: always | 1 | | qt, pl, chl, bi, rut, il |
| 89-27 | 79-146C[10,11]; 68-432M, U, D, A[9,10] | anthophyllite, gedrite, hornblende, cummingtonite | ortho: always | 1 | | qt, pl, st, cor, chl, rut |
| 89-31 | 73-22[11] | gedrite, hornblende, cummingtonite | none | none | | qt, pl, gar, bi, zir, st, chl, op |
| 89-32 | 73-24[11] | anthophyllite, gedrite, cummingtonite | ortho: sometimes | none | | qt, pl, gar, bi |
| 89-33 | 73-29D[9,10,11] | gedrite, hornblende | none | none | | cor, pl, qt, chl, bi, st, op |
| | | **Other localities** | | | | |
| 89-38 | None[G] | gedrite | always | none | 600–700 °C ~5–6 kbar | qt, pl, bi, rut |
| 9A-85 | DE-9[12] | gedrite | always | 1, 2 | 550 ± 70 °C ~3 kbar | qt, pl, chl, cor, gar, bi |
| FR-1 | M532[13] | gedrite | always | 2 | 640–710 °C ~3–5 kbar | cor, chl, gar, mag, bi, zir |
| GR-40 | [14] | gedrite | sometimes | none | ky-sil zone | qt, pl, cor, bi, rut |
| GR-41 | [14] | gedrite | sometimes | none | No *P* est. | |

[A] References: 1. Schumacher and Robinson (1986), 2. Schumacher (1988), 3. Schumacher (personal communication), 4. Robinson and Jaffe (1969a), 5. Robinson and Jaffe (1969b), 6. Robinson et al. (1971a), 7. Schumacher and Robinson (1987), 8. Gittos et al. (1976), 9. Spear (1980), 10. Spear (1982), 11. Spear and Rumble (1986b), 12. Earley and Stout (1991), 13. Gable and Sims (1969), 14. Heinrich and Rabbitt (1960).

[B] Orthoamphiboles with Si ≥ 7.0 are listed as anthophyllite, with Si < 7.0 as gedrite.

[C] The number 1 = {120} lamellar intergrowth, see Figs. 5, 6. The number 2 = Oxide inclusions, usually ilmenite or rutile along (100).

[D] *P-T* conditions at metamorphic peak, taken from the literature.

[E] Mineral abbreviations: qt = quartz, bi = biotite, st = staurolite, chl = chlorite, gar = garnet, ky = kyanite, sil = sillimanite, pl = plagioclase, rut = rutile, cor = cordierite, il = ilmenite, zir = zircon, mag = magnetite, op = unidentified opaques.

[F] The samples from this area were collected from outcrops at or near Spear's outcrops.

[G] From locality near Surry Mountain, from outcrop in Ashuelot River.

The petrology of these gneisses is described by Gable and Sims (1969).

Sample numbers, amphibole assemblages, and previous work for the orthoamphiboles used in this study are summarized in Table 1.

## TEM RESULTS

### The (010) and (120) exsolution lamellae

Many of the orthoamphiboles contained optically visible exsolution lamellae. These are most easily seen in basal sections under high magnification (see, e.g., Fig. 12 of Robinson et al., 1971a). Many other orthoamphiboles, however, appear homogeneous under the petrographic microscope. When examined with TEM, all of the orthoamphiboles contained exsolution lamellae.

Previous work on exsolved orthoamphiboles has shown two predominant orientations for exsolution lamellae, (010) and (120) (e.g., Ross et al., 1969; Gittos et al., 1976; Spear, 1980; Treloar and Putnis, 1982). The (010) orientation is far more common and has been observed for many years, whereas the (120) orientation was first discovered in a TEM study by Gittos et al. (1976), in amphiboles also examined in this study (locality 6A9 of Schumacher and Robinson, 1986). Figures 1 and 2 illustrate TEM images of the (010) lamellar orientation. Figure 1 shows coarse (010) lamellae of anthophyllite in a gedrite host. These lamellae are up to 200 nm thick and are optically visible in most cases. Note that there is some branching of lamellae, which was also observed by Gittos et al. (1976) in their TEM study. Figure 2 shows (010) lamellae of gedrite in an anthophyllite host. The exsolution lamellae are usually finer in the anthophyllite samples than in gedrite, consistent with previous studies (e.g.,

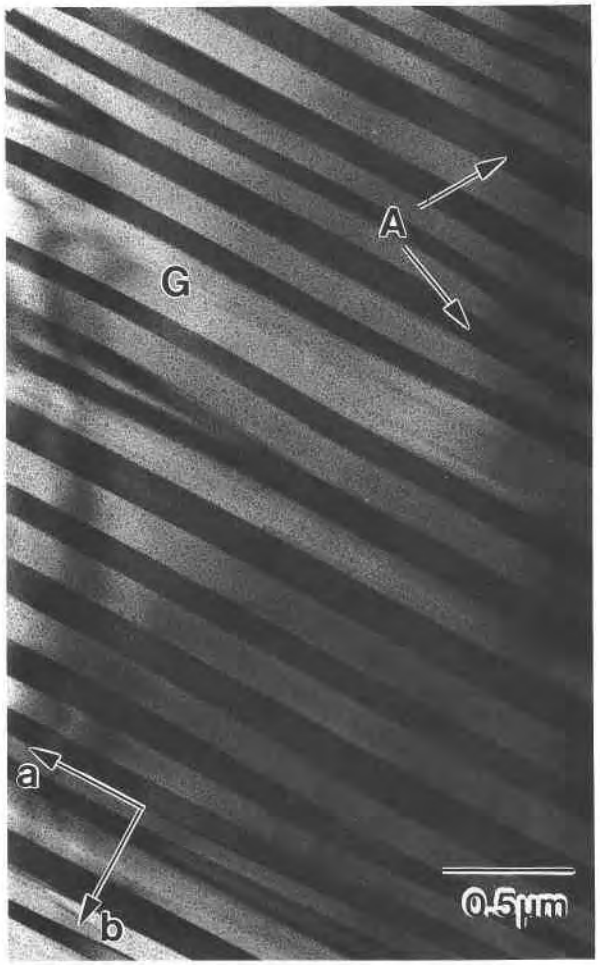


Fig. 1. Bright-field TEM image of coarse exsolution microstructure in gedrite. The anthophyllite lamellae are parallel to (010) and up to 200 nm in thickness. Note the interfaces with the gedrite host are relatively straight, although some lamellae show some branching. In this and all following micrographs, the gedrite areas are labeled "G" and the anthophyllite "A". The electron beam is parallel to [001]. Microstructure from sample FR-1.

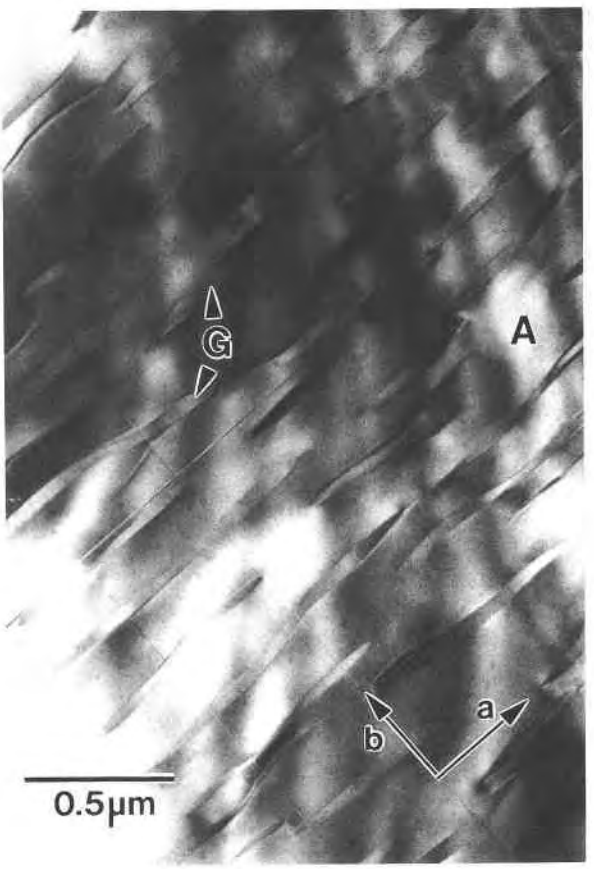


Fig. 2. Bright-field TEM image showing exsolution of gedrite from anthophyllite. These (010) lamellae are not as coarse as those in the gedrite samples and show more curved interfaces with the host. Note that the microstructure is cut by a series of (100) stacking faults. The electron beam is parallel to [001]. Microstructure from sample 89-18B.

Spear, 1980). Coarser exsolution textures, like those in Figure 1, generally consist of lamellae with nearly planar interfaces. Finer-scale textures show some deviation from planar morphology. Figure 3 shows an example of very fine (010) gedrite platelets known as Guinier Preston (GP) zones. GP zones are very common in most of the orthoamphibole samples examined in this study, usually occurring between larger lamellae (see below). They have also been observed in a variety of other exsolved amphiboles (e.g., grunerite-cummingtonite, Gittos et al., 1974; glaucophane cummingtonite, Smelik and Veblen, 1991).

Among the 17 samples studied, only two samples were found to contain abundant (120) lamellae. Figure 4 shows (120) lamellae of anthophyllite in gedrite in sample 89-2 (outcrop 6A9) from Amphibole Hill. These lamellae are also relatively coarse and in some cases could barely be seen under high magnification (400×) in doubly polished thin sections containing basal amphibole sections. This sample (89-2) and one other (6A9S) are from the same locality as the sample studied by Gittos et al. (1976), who showed the first example of this orientation. This (120) exsolution texture is pervasive in these orthoamphiboles, although deviations from strict (120) orientations were also observed.

Some of the samples showed unusual lamellar features parallel to (120) under high magnification in the petrographic microscope (Fig. 5), often accompanying normal (010) exsolution lamellae. Spear (1980, his Figs. 2b, 2c, 3b) observed similar optical discontinuities in his samples and interpreted these lamellae as growth-related features not related to exsolution. TEM examination of crystals like those shown in Figure 5 has shown that indeed these optical effects appear to be the result of lamellar intergrowths of orthoamphibole along (120) 1.5–2.5 $\mu$m in width, as shown in Figure 6. Note that the entire area also contains (010) exsolution lamellae of anthophyllite. The exsolution lamellae are less coarse in the central slab


Fig. 3. Bright-field TEM image showing homogeneously distributed Guinier Preston (GP) zones of gedrite in anthophyllite host. These tiny platelets are parallel to (010) and were common in most samples. The beam is near [001]. Microstructure from sample 89-18B.

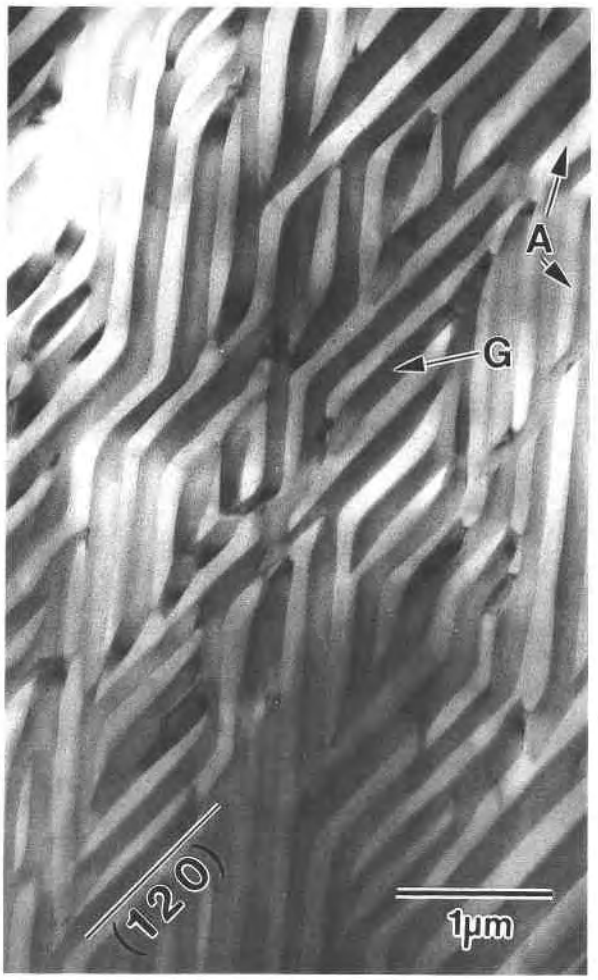


Fig. 4. Bright-field TEM image of pervasive {120} exsolution texture in Ca-rich orthoamphiboles from Amphibole Hill. This texture may represent a coarsened spinodal decomposition texture. The two orientations are related by symmetry. The electron beam is near [001]. Microstructure from sample 89-2.

of gedrite, compared with the slabs on either side, reflecting slightly different bulk compositions. HRTEM images show these amphibole slabs to be coherently intergrown with essentially no lattice rotation between the slabs. In many cases the exsolution textures were so pervasive that it became very difficult to identify these (120) slabs in the electron microscope once the sample was thinned.

### Unusual lamellar morphologies, new orientations, and the role of defects

In addition to the (010) and (120) orientations, other lamellar orientations have been observed in these samples. Figure 7 illustrates an area containing a single large (010) lamella surrounded by many smaller lamellae in a (130) orientation. Analytical electron microscopy (AEM) has shown no compositional difference (within analytical error) between the two types of lamellae. Because the (010) lamella is significantly larger than the (130) lamellae, it may be that the (010) orientation was favored at slightly higher temperatures; then during continued slow cooling, the (130) orientation became more stable as exsolution began in the surrounding areas. In some samples the exsolution lamellae have curved orientations that straddle (010) (Fig. 8).

Coarsened exsolution textures like those in Figures 1, 4, and 8 are enigmatic when it comes to determining the exsolution mechanism responsible for the microstructure. These areas may represent a coarsened spinodal decomposition texture, or they may be the result of nucleation and growth processes, a problem discussed later in the paper.

In many of the samples, areas were found that contained lamellae possessing unusual morphological characteristics. In these cases, structural defects appear to play an important role in the development of the lamellar morphology, as first suggested by Gittos et al. (1976). Figures 9 through 11 show typical examples of unusual lamellae.

Figures 9 and 10 show unusual lamellar morphologies associated with (010) amphibole CWEs. In the vicinity

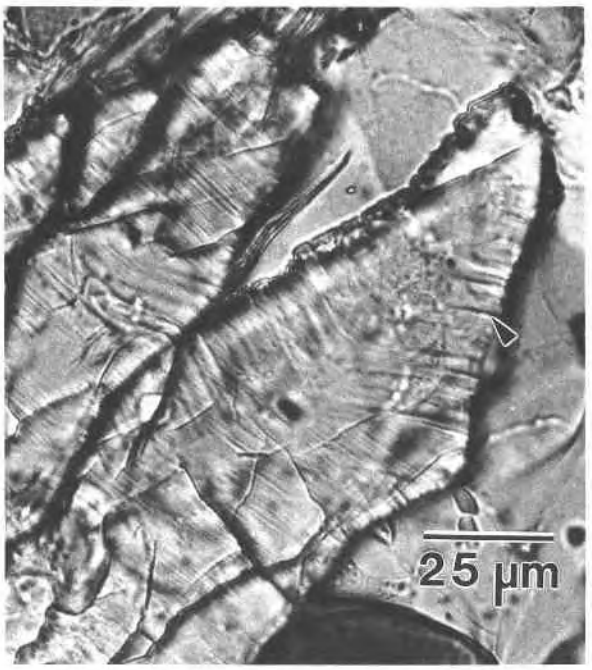


Fig. 5. Plane-light optical micrograph of (001) orthoamphibole grain in sample 9A85. This gedrite crystal shows very narrow (010) exsolution lamellae (fine striations bisecting obtuse cleavage angle) and larger {120} features (arrow). These {120} features result from a lamellar intergrowth of orthoamphibole slabs along (120) thought to form during primary amphibole growth.

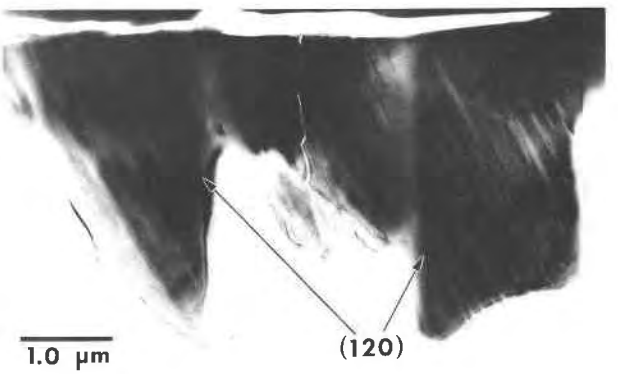


Fig. 6. Bright-field TEM image of ion-thinned amphibole grain containing {120} lamellar growth features. The orthoamphibole slabs are about 2.0 μm wide and are bounded by (120) planes. The intergrowth is coherent with essentially no lattice rotation between adjoining slabs. All three slabs shown here contain (010) exsolution lamellae of anthophyllite, which make about a 25° angle with the (120) interface. The exsolution lamellae in the central slab are narrower, reflecting a slightly different bulk composition. The crack across the top of the image is a {210} cleavage crack. The electron beam is near [001]. Microstructure from sample 9A85.

of the terminations of the narrow zippers of wide-chain material there is considerable strain contrast in the images, which is caused by the incoherent nature of the terminations. Figure 10 is a [001] HRTEM image of a single anthophyllite lamellae forming along a CWE in gedrite. Note that the contrast between the lamella and host is very subtle; therefore an inset is provided with the lamellar boundary outlined. The CWE consists of a strip of quintuple-chain material, entering from the bottom of the image and terminating where it meets another small defective area that involves the loss of a single subchain of gedrite from the top. Note that precipitate growth is impeded in the vicinity of the defect termination; thus the defect is effectively pinning the lamellar boundary. The structural distortion and character of the defect can be seen best by viewing along the (010) fringes at a low angle. For a complete discussion of (010) planar defects in amphiboles, see the papers by Veblen and Buseck (1979, 1980).

There are two important morphological characteristics to consider. First, surrounding the terminations of the narrow zippers of wide-chain material, there is considerable bulging of the exsolution lamellae (Fig. 9). The widening of the lamellae at these locations may be due to enhanced cation diffusion along the wide structural tunnels created by the structural mismatch in the local area of the zipper terminations. This fast diffusion process has been suggested by Veblen and Buseck (1980) and Veblen (1991) as operating during lamellar polysomatic reactions in pyriboles, and the TEM images of these exsolved orthoamphiboles suggest that this process may also have an influence on exsolution reactions.

The second interesting feature is the occurrence of embayments in the exsolution lamellae (Figs. 9, 10, 11). Embayed regions always occur in the local areas of zipper terminations (Figs. 9, 10, 11A) or at the terminations of (100) stacking faults (Fig. 11B). CWE terminations are in some ways similar in structure to edge dislocations, and in the same way that dislocations can affect grain boundary mobilities, the CWE terminations appear to influence the movement of lamellar interfaces. This boundary pinning effect is especially pronounced in the large embayments associated with the anthophyllite lamella shown in Figure 11A. This large lamella has yet a new orientation, near (140), and contains three short sections of triple-chain material. Both ends of two of these short zippers terminate within the lamella at the innermost reaches of deep embayments, pinning the lamellar interfaces there. The walls of the embayments have ($1\bar{4}0$) orientations. In Figure 11B, similar embayments have developed in association with the terminations of (100) stacking faults. These stacking faults represent narrow strips of monoclinic amphibole and have been observed in previous orthoamphibole studies (Gittos et al., 1976; Treloar and Putnis, 1982). The lamellae of anthophyllite in Figure 11B have somewhat curved orientations straddling (010), with additional triangular domains of anthophyllite forming opposite the embayments at the (100) fault terminations. These triangular domains clearly appear to

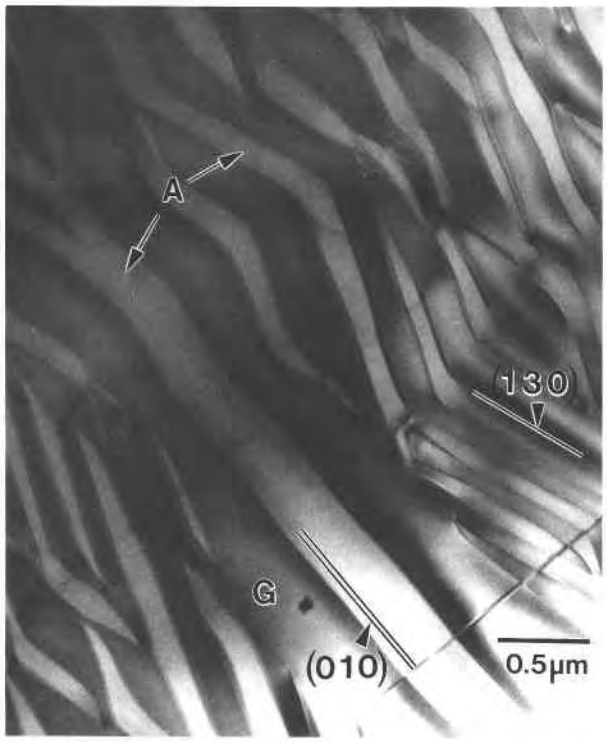


Fig. 7. Bright-field TEM image of two lamellar orientations in one small area. The large (010) lamella probably formed earlier than the network of {130} lamellae. The entire microstructure is cut by a series of narrow (100) faults. The electron beam is near [001]. Microstructure from sample 6A9S.

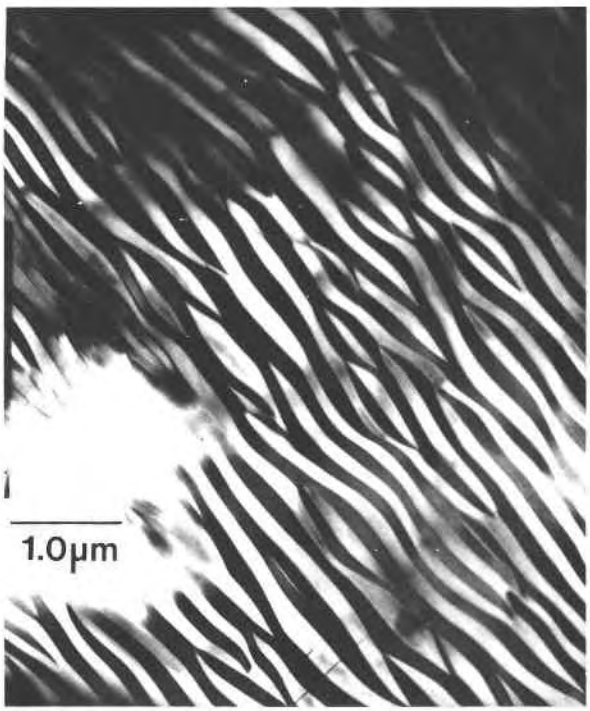


Fig. 8. Bright-field TEM image showing pervasive exsolution texture consisting of curved lamellae straddling (010) planes. The dark lamellae are gedrite and the light lamellae are anthophyllite. Note branching and forking of lamellae. The electron beam is near [001]. This texture may represent a coarsened spinodal decomposition texture. Microstructure from sample 7A7L.

have formed after the stacking faults, whereas at least some of the larger lamellae seem to predate the faults (e.g., note the lamella at the bottom of Fig. 11B). From the above observations, it seems likely that the inability of the precipitate to grow in the vicinity of the defect terminations may be due to the strain field surrounding the locally distorted crystal structure near the terminations. Strain-field interactions have been suggested by Livi and Veblen (1989) as being partially responsible for unusual lamellar morphologies in pyroxenes, especially the bulging of lamellae as they approach one another. In this case, however, the defects and their associated strain fields appear to play two roles; in some regions, the lamellar boundaries are pinned by the defect, whereas in adjacent areas the strain and the defect structure may contribute to the lamellar bulging.

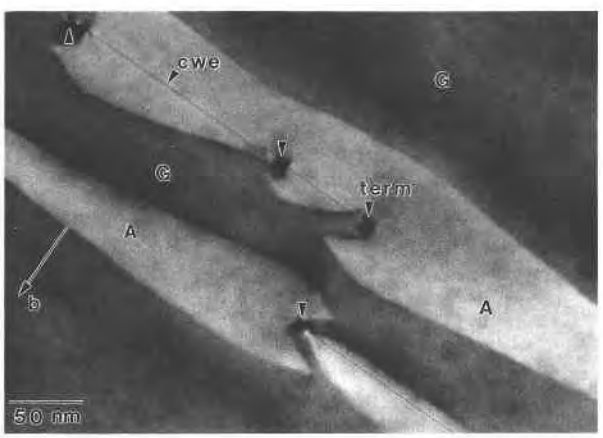


Fig. 9. High-magnification [001] image of unusual lamellar morphologies associated with the terminations of (010) CWEs. Note the bulging of the anthophyllite lamellae near the defect terminations. This may be due in part to enhanced chemical diffusion along the wide structural channelways created by the planar defects. Also note the unusual embayments that occur in the vicinity of the CWE terminations. These are thought to be the result of high lattice strain in these areas, which causes boundary pinning of the lamellar interfaces. Microstructure from sample 89-31.

### Evidence for progressive exsolution

In many of these samples there is abundant evidence for progressive or continual exsolution during slow cooling of the host amphibole. This evidence is in the form of several types or scales of exsolution lamellae in a single area of a crystal. Figure 12 is a TEM image showing three generations of exsolution lamellae in gedrite. The three large (010) anthophyllite lamellae undoubtedly grew first and appear to be the result of heterogeneous nucleation

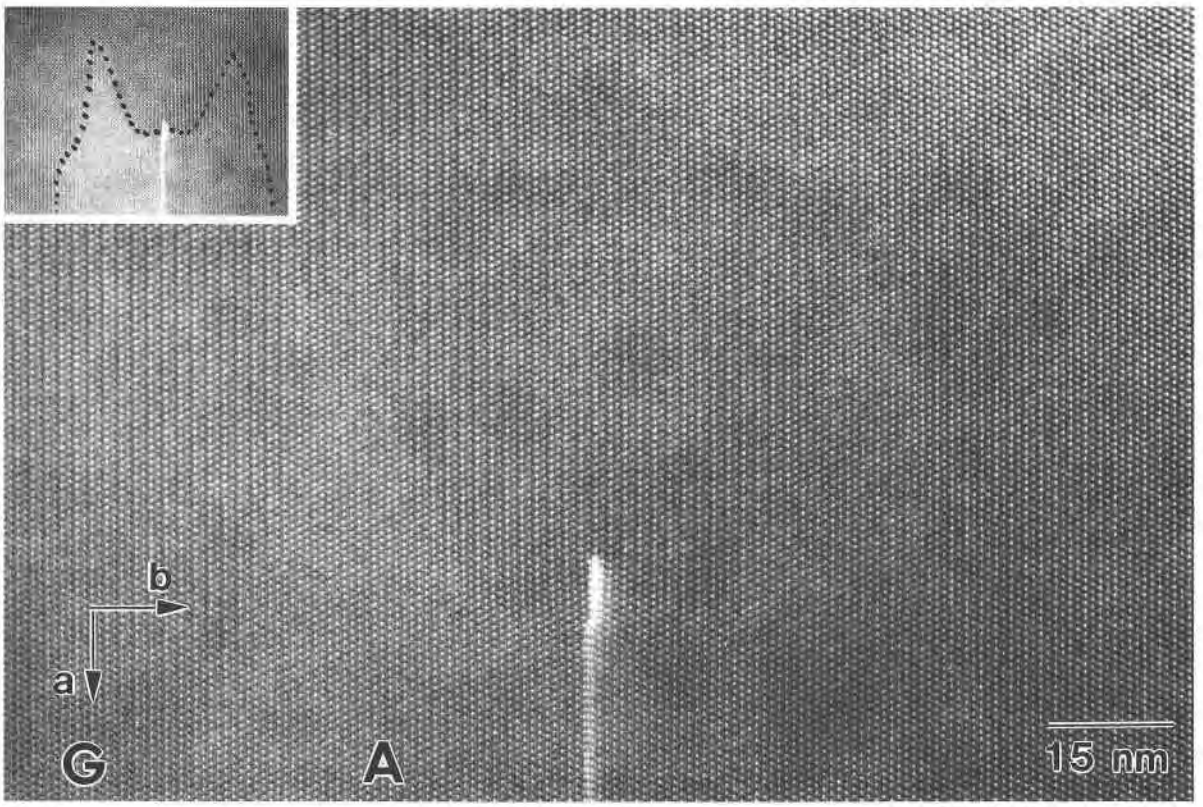


Fig. 10. HRTEM image taken down [001] of an embayment occuring at an incoherent CWE termination. The inset shows the approximate shape of the anthophyllite lamella. By carefully sighting parallel to the (010) lattice fringes, it may be seen that this termination is complex, involving a strip of quintuple-chain material entering from the bottom of the image and meeting a defective area where there is a loss of a 0.9-nm slab (a single subchain) of gedrite from the top part of the image. Microstructure from sample 89-32.

and growth along (010) CWEs (see arrows in Fig. 12). It is quite common for large lamellae like this to contain CWE running their entire lengths, and in other cases (Fig. 13) the evidence for nucleation along these defects is even more clear-cut. In many cases, HRTEM images showed that the defects are located at the very centers of the exsolution lamellae.

As seen in Figure 12, exsolution continued as the mineral cooled further, as evidenced by the medium-sized (010) lamellae in the upper left of the image. Note that these lamellae are more curved than the large lamellae. The regions between the large lamellae show even smaller lamellae, and this overall texture reflects the development of a strong compositional gradient across this amphibole

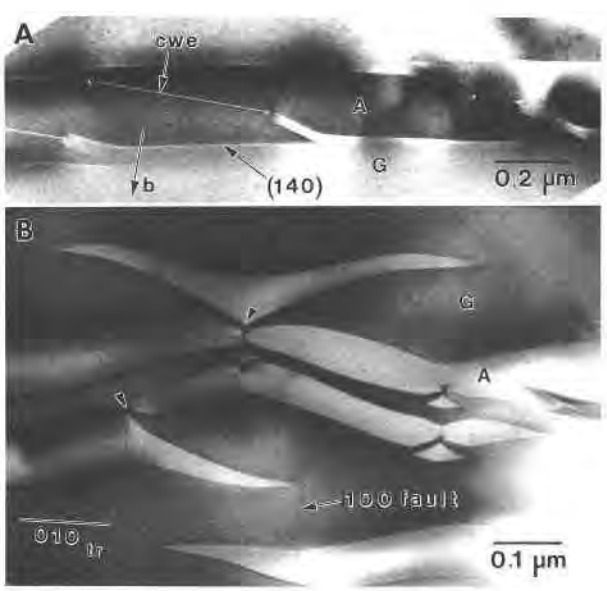


←

Fig. 11. (**A**) Bright-field TEM image of a large anthophyllite lamella containing deep embayments associated with terminations of short sections of (010) wide-chain silicate. The large lamellae has a (140) orientation, and the inside walls of the embayments have a ($1\bar{4}0$) orientation. The electron beam is near [001]. Microstructure from sample W95. (**B**) Unusual morphologies associated with (100) stacking faults. Note the embayments and the unusual triangular-shaped anthophyllite domains. These triangular domains appear to have postdated the faults, whereas some of the larger curved lamellae appear to predate the faults. The trace of (010) is shown for reference. The electron beam is near [001]. Microstructure from sample 6A9S.


Fig. 12. Bright-field TEM image showing evidence for continual exsolution during cooling. The large straight lamellae formed first, nucleating on (010) CWEs, which run their entire length. As cooling progressed, the regions between the large lamellae became supersaturated with anthophyllite component. The region to the upper left of the image contains coarser lamellae than the areas between the large lamellae, and nucleation probably began in this area slightly before the nucleation of the smallest lamellae. The electron beam is near [001]. Microstructure from sample 89-27.

grain during exsolution. As the mineral cooled, regions between large lamellae having a higher concentration of solute became supersaturated and undercooled enough for exsolution to begin. The actual temperature changes recorded in the texture are, of course, unknown and in fact may be quite small. These areas of smaller lamellae are usually defect free and probably formed by homogeneous nucleation and growth processes. These textures probably reflect the relationship between the chemical solvus and the coherent solvus in this system. Similar textures, with fine-scale precipitates between early-formed exsolution lamellae, are observed in other silicates, such as pyroxenes (see e.g., Fig. 11 of Champness and Lorimer, 1976).

Figure 14 shows another area displaying two types of exsolution lamellae resulting in a different texture from that shown in Figure 12. First there is an array of medium-sized, lens-shaped lamellae that are approximately 400–500 nm in their long dimensions. Some of these are associated with defects and some are defect-free, and they all probably nucleated before the development of the finer exsolution texture. The second type of texture occurs as abundant fine-scale GP zones that formed in the solute-rich areas between the larger lamellae. Note the distinctive football shape of the solute-depleted zones around the larger lamellae. The geometry of these precipitate-free regions reflects the diffusion and growth process, with maximum diffusion occurring in a direction normal to the lamellar interface and maximum growth along the length of the lamellae. Figure 15 shows a last example, with evidence for up to 5 scales of exsolution in a single small area. The large (010) anthophyllite lamella with the CWE running down its center represents the start of the exsolution process. This was followed by the medium-sized lens-shaped lamella in the center part of the micrograph. Another of these formed just to the left of the larger. Then, as cooling progressed, there was abundant heterogeneous nucleation of platelets along (100) stacking faults and homogeneous nucleation of GP zones in the remaining solute-enriched areas during the final stage of exsolution. Most probably this progression of exsolution was continuous during cooling, rather than a series of discrete precipitation events, and the actual cooling interval was small.

The (100) stacking faults shown in the above images have been observed in every sample examined in this study and were observed by Gittos et al. (1976) in their TEM study of orthoamphibole. Treloar and Putnis (1982) presented an HRTEM image of one of these faults in anthophyllite from Finland, viewed down the **b** axis, showing that they represent narrow strips of monoclinic amphibole within the orthoamphibole. Figure 16A is a similar HRTEM image of a single (100) stacking fault viewed down [011] in anthophyllite. In the orthorhombic material, the zig-zag pattern reflects the regular alternation of octahedral stacking (++−−++−− . . .) along the **a** axis. The (100) defect represents a break in this stacking sequence with the introduction of a narrow strip

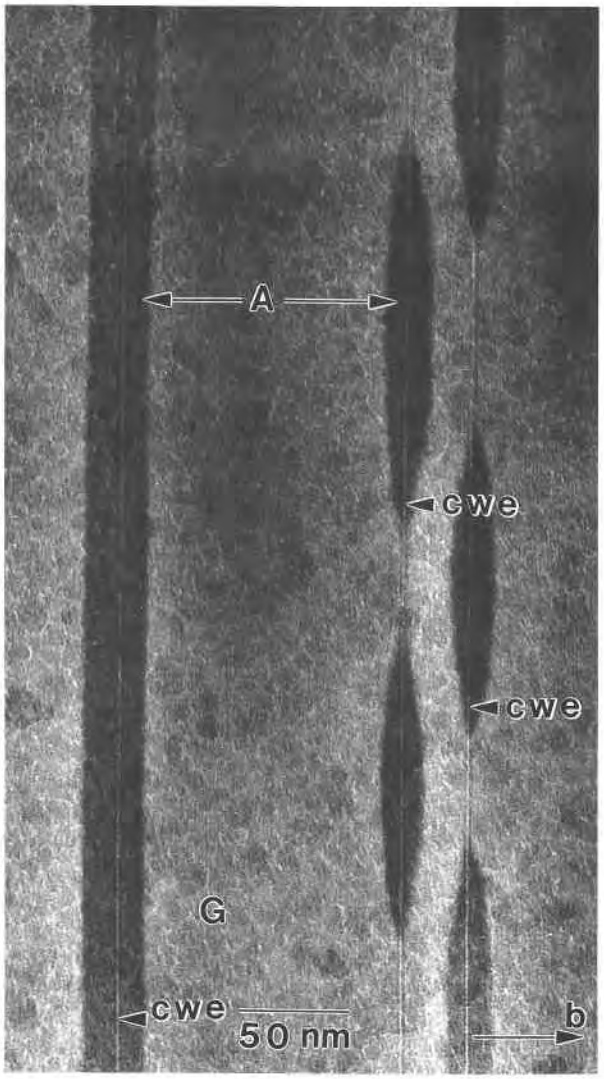


Fig. 13. Bright-field TEM image showing early stages of heterogeneous nucleation of anthophyllite lamellae along (010) CWEs. With further coarsening, these disk-shaped lamellae would probably coalesce into large planar lamellae similar to the one at the left of the image. The electron beam is near [001]. Microstructure from sample 89-32.


Fig. 14. Bright-field TEM image showing evidence for two types of exsolution lamellae in gedrite. The first is represented by the medium-sized disk-shaped lamellae. With additional cooling, there was rapid homogeneous nucleation of abundant GP zones in the solute-enriched areas between the bigger lamellae. Note the distinctive football-shaped solute depletion zones around the larger lamellae. Versions of this texture were common in many of the samples. Beam is near [001]. Microstructure from sample 89-32.

of monoclinic amphibole (++++ . . .) two unit cells wide. Figure 16B is an [001] HRTEM image of several of these faults cutting across a large anthophyllite lamella in gedrite (see arrows). In this **ab** projection the $b/2$ component of the $n$-glide relationship in (100) between the clino- and orthoamphibole lattices can be seen in the $b/2$ offset of the (010) lattice fringes throughout the image. Growth ledges along the anthophyllite gedrite interface at these fault locations can also be seen. Faults of this sort have been studied in detail for the orthopyroxene-clinopyroxene system by many authors (e.g., Iijima and Buseck, 1975, 1976; Coe and Kirby, 1976; Kirby, 1976; McLaren and Etheridge, 1976) and are typically attributed to deformation. A detailed analysis of deformation mechanisms involving unit-cell twinning and faulting along (100) has not yet been carried out for these amphiboles, but it seems likely that the mechanisms are analogous to those in pyroxenes.

The TEM images presented above represent typical examples of exsolution microstructures and associated defect structures observed in these amphiboles. Because of the large number of samples studied, every variation in exsolution style cannot be presented here. All the TEM results, however, are summarized in Table 2, which lists the sample numbers and localities, plus descriptions of the exsolution textures and orientations observed for all the samples.

## Optimal phase boundary calculations

The TEM results presented above and summarized in Table 2 indicate that the orientations of exsolution lamellae in orthoamphiboles range from planar (010) lamellae (Fig. 1) at one extreme, through curved lamellae straddling (010) (Fig. 8), (140) lamellae (Fig. 11A), (130) lamellae (Fig. 7), to (120) lamellae at the other extreme (Fig. 4), with irrational orientations occurring between

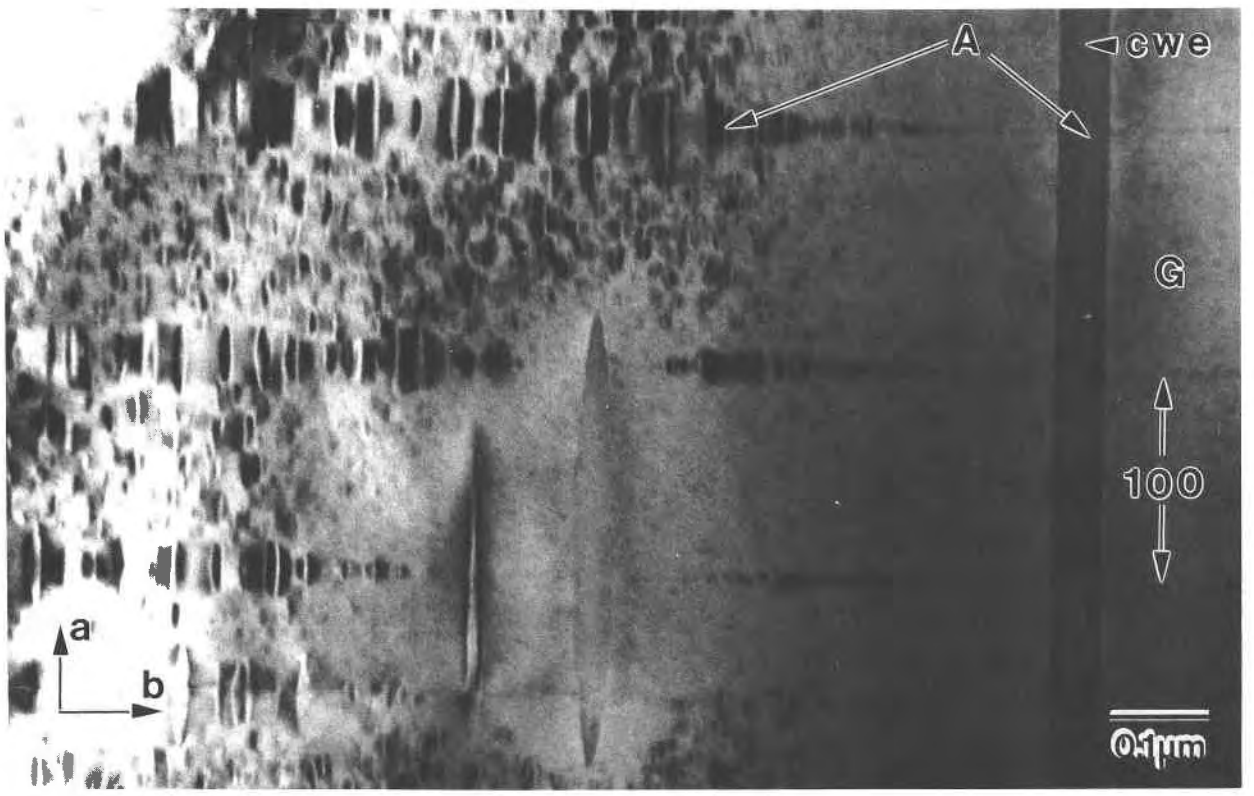


Fig. 15. Bright-field TEM image showing evidence for progressive exsolution in gedrite. The large (010) lamella containing a CWE at its center probably nucleated early on, followed by the medium-sized disk-shaped lamella near the center of the image. A second one of these, a bit smaller and just to the left of the larger one, can also be seen. With additional cooling, heterogeneous nucleation of small precipitates occurred along a series of (100) stacking faults (labeled), while homogeneous nucleation of fine GP zones in the solute enriched areas between the other lamellae took place. It seems likely that this overall texture developed by continuous nucleation and growth during slow cooling. The electron beam is parallel to [001]. Microstructure from sample 89-32.

the rational ones. The morphologies of the precipitates are further modified by the presence of planar defects as shown above.

It has been well established that one of the primary factors governing the orientation of exsolution lamellae in chain silicates is the dimensional or structural misfit between the lattices of the two minerals, with the interface usually adopting an orientation representing the minimum interfacial strain energy or best fit between the two structures (e.g., Robinson et al., 1971b; Jaffe et al., 1975; Robinson et al., 1977; Fleet et al., 1980; Fleet, 1982; Smelik and Veblen, 1991). Following the nomenclature of Bollman and Nissen (1968), these minimum-strain or best-fit interfaces have been termed optimal phase boundaries.

In an effort to understand what subtle differences may control the various orientations for exsolution lamellae in orthoamphiboles, three-dimensional optimal phase boundary calculations for coherently intergrown anthophyllite and gedrite were performed. The calculations were done using the three-dimensional lattice-fitting program (EPLAG) of Fleet (1982, 1984). This version of EPLAG calculates only the area misfit between normalized equivalent (*hkl*) planes in the two related lattices and makes no quantitative estimate of elastic strain energy. The area strain (misfit) was calculated at grid points on a hemisphere about the **b** axis using a grid interval of 5°. Each grid point corresponds to a stereographic pole of an interatomic plane (*hkl*) and is described in terms of the spherical coordinates $D$ and $E$, where $D$ is a counterclockwise rotation about **b** and $E$ is a clockwise rotation about an axis normal to **b** (see Fleet, 1982, for details of the 3-D theory). The results are displayed on a stereographic projection down **b**, the equatorial plane being the **a*c*** reciprocal lattice plane (which is the same as the **ac** plane for orthorhombic minerals).

The calculations make use of unstrained lattice parameters that were obtained from the literature. The anthophyllite unit-cell parameters were taken from the structure refinement data of Finger (1970). Two gedrite cells were chosen from the X-ray work of Papike and Ross (1970). The cell parameters are given in Table 3. Gedrite 2 is sample I34I of Robinson and Jaffe (1969a, 1969b) from the Amphibole Hill area. Previous XRD work by

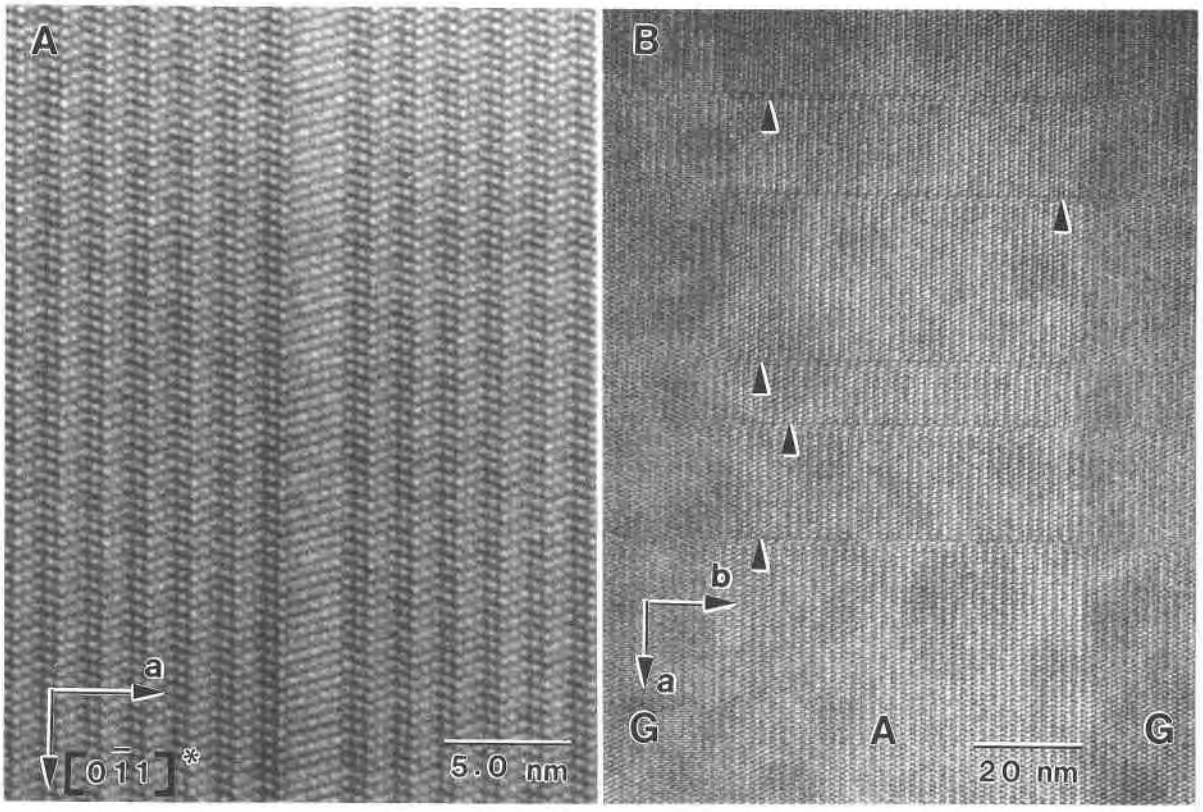


Fig. 16. (**A**) HRTEM image of a single (100) stacking fault in a homogeneous region of anthophyllite. The image is taken down [011]. The regular alternation of octahedral stacking (++−−++−−) along **a** can easily be seen by the zig-zag pattern in the orthorhombic material. The fault represents a narrow strip of monoclinic material formed by an error in this stacking sequence. The monoclinic area is only two unit cells thick. AEM could detect no compositional difference, so this feature should be considered a polymorphic intergrowth of cummingtonite in anthophyllite along (100). These features are thought to form as the result of deformation. Microstructure from sample 89-18B. (**B**) HRTEM image taken down [001] showing a series of (100) stacking faults (arrows) cutting across a large anthophyllite lamella in gedrite. By sighting down the (010) lattice fringes the offset of $b/2$ produced by these faults can easily be seen. Growth ledges along the lamellar-host interface in the vicinity of these faults can also be seen. Microstructure from sample FR-1.

Ross et al. (1969) and electron diffraction work by Christie and Olsen (1974) on exsolved orthoamphiboles have indicated that the $a$ and $c$ unit-cell parameters of the two amphiboles are identical, whereas the $b$ axial lengths may differ by as much as 2%. Clearly, in every case where $a$ and $c$ are truly identical, one would expect only (010) exsolution lamellae. Treloar and Putnis (1982), in their TEM study of exsolved gedrite containing (010) exsolution lamellae of anthophyllite, observed no splitting of (0$k$0) reflections, as would be expected. In this study, splitting of reflections along **b*** in [001] selected-area electron diffraction (SAED) patterns was always observed, especially when the lamellae were coarse. Note from Table 3 that the unit-cell parameters used for the optimal phase boundary calculations do not possess identical $a$ and $c$ axes. The variable orientations observed in this study suggest that although the difference in $b$ axial lengths exerts a strong control on the lamellar orientation, small differences in $a$ and $c$ lead to deviations from strict (010) orientations. The results from the EPLAG calculations show remarkable support for this hypothesis.

Figure 17 summarizes the results from the EPLAG calculations for the two orthoamphibole pairs considered. In Figure 17A the results are displayed on a stereographic projection down **b**. For reference, poles for (100), (001), (010), and (120) are shown. Also shown is a shaded area meant to represent the range of orientations observed in this study. The calculated plane of best fit for the first pair, anth-ged1, was exactly at (010). This is not surprising, considering the relative differences in lattice parameters. For this pair, the $b$ axes differ by a large value of 1.5% (0.0272 nm). The difference in $a$ is small (0.16%) and although the percentage difference in $c$ axes is substantial (0.62%), the magnitude of the difference is small (0.0033 nm) compared with $\Delta b$ and therefore has no effect on the calculated phase boundary. The calculated optimal phase boundary for the second pair, anth-ged2, is remarkably close (within 1°) to (120), as shown in Fig-

**TABLE 2.** Summary of exsolution microstructures in orthoamphiboles

| Sample, this study* | Observed exsolution textures** | Predominant lamellar orientation | Other observed orientations | Exsolution mechanisms† | Defects observed | |
|---|---|---|---|---|---|---|
| | | | | | (100) faults | (010) CWE |
| | | | **Amphibole Hill** | | | |
| 7A0BX | a, b, 3, 9, 10 | (010) | none | 1, 2 | rare | rare |
| 7A7H2 | a, b, c, 3, 15 | (010) | none | 1, 2 | common | rare |
| 7A7L | 8, 9, 10, 11b | curved "010" | (010) | 1, 2, 3 | common | rare |
| 7A7J | a, b, c, d, 3, 14, 15 | (010) | none | 1, 2 | common | common |
| W95 | 1, 2, 3, 9, 10, 11a, 12 | (010) | (140) | 1, 2 | common | common |
| 6A9S | 3, 4, 7, 11b | (120), (130) | (010), curved "010" | 1, 2, 3 | abundant | rare |
| 89-2 | 4, 7, 11b | (120), (130) | (010), curved "010" | 1, 2, 3 | abundant | rare |
| | | | **Post Pond area** | | | |
| 89-18B | 1, 2, 3, 5, 6, 12, 16 | (010) | curved "010" | 1, 2 | abundant | common |
| 89-27 | 1, 2, 3, 12 | (010) | (130) | 1, 2 | rare | common |
| 89-31 | a, d, 3, 9, 10, 12, 13 | (010) | curved "010" | 1, 2 | common | common |
| 89-32 | 3, 9, 10, 13, 14, 15 | (010) | curved "010" | 1, 2 | common | abundant |
| 89-33 | a, 2, 3, 13 | (010) | curved "010" | 1, 2 | rare | common |
| | | | **Other localities** | | | |
| 89-38 | 1, 3, 12 | (010) | curved "010" | 1, 2 | rare | common |
| 9A-85 | 1, 2, 3, 5, 6, 9, 10, 16b | (010) | curved "010" | 1, 2 | abundant | abundant |
| FR-1 | 1, 3, 9, 10, 16b | (010) | curved "010" | 1, 2, 3 | abundant | common |
| GR-40 | 1, 3, 12, 14 | (010) | curved "010" | 1, 2 | common | common |
| GR-41 | d, 3, 9, 10, 12, 13, 14 | (010) | curved "010" | 1, 2 | common | common |

* For corresponding literature samples and references see Table 1.

** The numbers refer to figures in the paper showing similar textures, except for a = considerable regions of homogeneous orthoamphibole, b = scattered small lamellae nucleating on dislocations or stacking faults, c = heterogeneous nucleation along interfaces of oxide inclusions, d = heterogeneous nucleation at subgrain boundaries.

† The number 1 = heterogeneous nucleation and growth, 2 = homogeneous nucleation and growth, 3 = possible coarsened spinodal decomposition texture.

ure 17. When one considers the unit cells for this pair (Table 3), the difference in $b$ is still the largest (0.97%), but considerably smaller than for the first pair, the difference in $c$ is very small, and the difference in $a$ is relatively small (−0.22%), but larger than in the first pair.

Because the observed orientations and the calculated orientations all belong to the [001] zone [having ($hk$0) indices], another way to present the EPLAG results is by plotting the area misfit values vs. the $E$ spherical coordinate at a constant $D$ coordinate of 90°. This effectively projects the results from the **ab** plane onto the **a*−a*** line, as shown by the base of Figure 17B. For the first pair, a single misfit minimum is seen at $E$ = 90°, or (010). The second pair shows two minima, however, related by symmetry, at (120) and ($\bar{1}$20). Note that the orientations between the minima [(010), (130), etc.] show a higher area misfit.

It is interesting, and totally fortuitous, that these two pairs reproduce exactly the two end-member orientations observed in this, and other, studies. These results strongly suggest that the true lamellar orientations in orthoamphiboles will be determined mostly by the combined relative differences in the $a$ and $b$ axial lengths. As the difference in $a$ becomes larger, especially when coupled with decreases in the difference between $b$ axes, the lamellar orientations progressively change from (010) to (120). The differences in $c$ would have to be very substantial for the lamellar orientations to occur in a zone other than [001] [i.e., have indices other than ($hk$0)]. The actual differences in unit cells are, of course, largely dependent on the actual chemical compositions (site occupancies) of the amphiboles (as well as temperature). The study of Colville et al. (1966) has shown the $b$ axial lengths in amphiboles to be quite sensitive to compositional changes, especially the occupancies of M4 and M2. The large amount of Al in M2 of gedrite, compared with (Mg-Fe) in anthophyllite, explains why the $b$ axis of gedrite is always shorter than that of anthophyllite. The structure refinements of anthophyllite (Finger, 1970) and gedrite

**TABLE 3.** Unit-cell parameters and site occupancies for orthoamphiboles used in EPLAG calculations

| | Anthophyllite (Finger, 1970) | Gedrite 1 (Papike and Ross, 1970) | % Diff. anth. | Gedrite 2 (Papike and Ross, 1970) | % Diff. anth. |
|---|---|---|---|---|---|
| | | **Unit-cell parameters** | | | |
| $a$ | 1.856 nm | 1.8531 nm | 0.156 | 1.8601 nm | −0.221 |
| $b$ | 1.8013 nm | 1.7741 nm | 1.51 | 1.7839 nm | 0.966 |
| $c$ | 0.52818 nm | 0.5249 nm | 0.621 | 0.5284 nm | −0.042 |
| | | **Occupancies for M4 sites** | | | |
| $Fe^{2+}$ | 1.022* | 0.84** | | 1.3** | |
| Mg | 0.888* | 1.1 | | 0.64 | |
| Ca | 0.09* | 0.04 | | 0.04 | |
| Na | | 0.02 | | 0.02 | |
| | | **Occupancies for M2 sites** | | | |
| $Fe^{2+}$ | 0.044* | 0.08** | | 0.18** | |
| Mg | 1.956* | 0.72 | | 0.46 | |
| Al | | 1.2 | | 1.36 | |
| | | **$Fe^{2+}/(Fe^{2+} + Mg + Mn)$** | | | |
| | 0.168 | 0.201 | | 0.425 | |

* Site occupancies adjusted based on reanalysis of this anthophyllite sample (by Seifert and Virgo, 1974, 1975; see Hawthorne, 1983, p. 417).

** Fe given as ($Fe^{2+}$ + $Fe^{3+}$ + Mn + Ti).

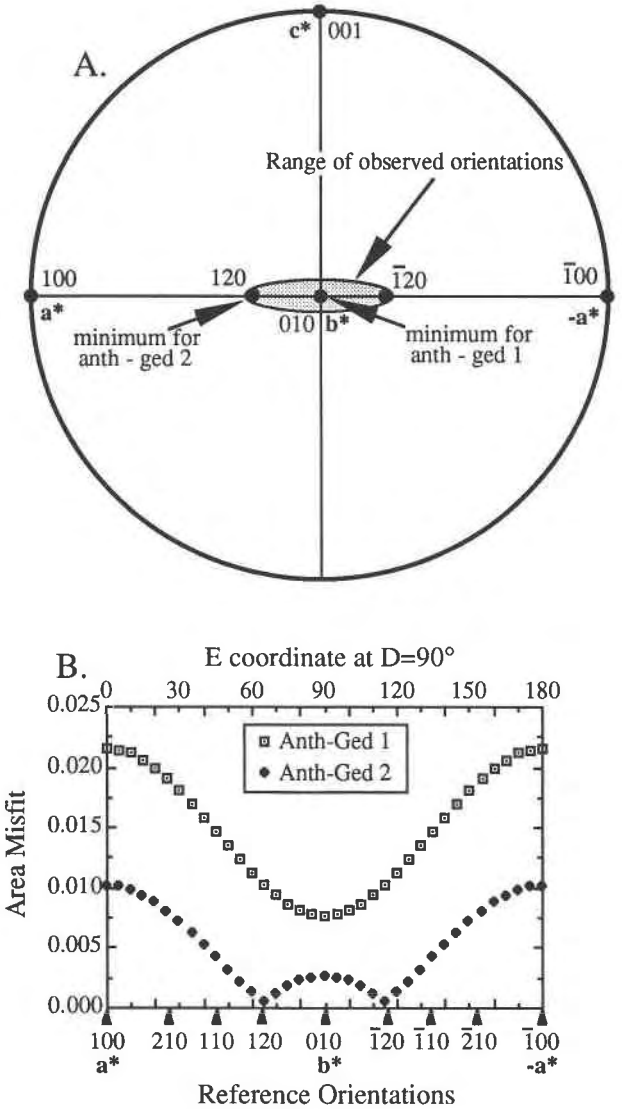


Fig. 17. (**A**) Stereographic projection down **b** showing results from optimal phase boundary calculations using EPLAG for intergrown anthophyllite gedrite. The poles for (010), (100), (001), and (120) are shown for reference. The stippled area is meant to represent the range of observed orientations for the orthoamphiboles. The calculated optimal phase boundary for the pair anth-ged1 is exactly at (010) because of the large $\Delta b$ between the two lattices (see Table 3). For the second pair, anth-ged2, the calculated minimum was remarkably close (within 1°) to (120). This is due to a decrease in $\Delta b$ coupled with an increase in $\Delta a$, which changes the optimal phase boundary from (010) to (120). (**B**) This diagram shows a plot of the calculated area misfit values vs. the $E$ coordinate value at a constant $D$ value of 90°. This projects the data onto the **a***−**a*** line in **A**. Note that for the first pair there is a single minimum at (010), whereas for the second pair there are two minima, at (120) and ($\bar{1}$20) (related by symmetry), with an increasing area misfit at orientations between the minima [(010), (130), etc.]. These two orientations, (010) and (120), represent end-member orientations for exsolution lamellae in orthoamphiboles.

(Papike and Ross, 1970) and the Mössbauer spectroscopy study of Seifert (1977) have shown that in the anthophyllite gedrite series the larger $Fe^{2+}$ ion is generally more strongly ordered into the M4 site than is Mg, although the partitioning of Fe and Mg among the octahedral sites can be complex. For example, M4 in orthoamphiboles always contains significant Mg, a factor probably responsible for the orthorhombic structure type (Hawthorne, 1983). In addition, any Ca in the analysis, and possibly some Na, would also be expected to occur at M4.

The site occupancies for the three amphiboles, from the structure refinements, are also shown in Table 3. Ged1 is very poor in Fe (1.14 cations pfu) and therefore has significant Mg in M4 (Table 3). This serves to shorten the $b$ axis of ged1, which explains the large difference between the $b$ axes in the first pair, and the (010) optimal phase boundary. In ged2, the higher Fe/Mg ratio leads to more $Fe^{2+}$ in M4 and a longer $b$ axis. This suggests that all magnesian gedrite and magnesian anthophyllite should develop exsolution lamellae parallel to (010), whereas those richer in Fe may develop ($hk$0) lamellae, depending on the actual differences in the $a$ axes. Both gedrite samples have small amounts of Ca and Na assigned to M4, which will also lengthen the $b$ axes (Colville et al., 1966).

The bulk analyses for orthoamphiboles from locality 6A9 (Amphibole Hill) presented by Robinson et al. (1971a) indicate an even higher Ca content than those used in the EPLAG calculations (~0.112 Ca pfu). The effect of Ca in this case is to lengthen the $a$ axis a small amount, which, in combination with decreases in $\Delta b$, leads to the (120) and (130) orientations, even in samples with relatively low Fe/Mg ratios.

## Analytical electron microscopy

Energy-dispersive X-ray analyses were obtained for all exsolved phases using a very fine probe (10–20 nm). Where possible, the sample was oriented in the sample holder with the **b** axis nearly parallel to the axis of the goniometer $x$-tilt. This usually allowed specimen tilting in the **ac** plane with minimal $y$ tilt. This way, the goniometer could be tilted into an optimal analytical orientation, and at the same time the lamellae would remain in nearly edge-on orientations. This geometry reduced the likelihood of analytical contributions from surrounding areas when analyzing small precipitates or the host between them. All amphibole formulae have been reduced on a 23-O basis, assuming all Fe as FeO, and site assignments have been made following Robinson et al. (1982). Analyses of both exsolution lamellae and host compositions from between lamellae were obtained for each exsolved sample. The paper by Robinson et al. (1971a) stresses the great importance of Na in the A site of orthoamphibole, and it is reemphasized that estimation of A-site occupancies using AEM data can be very uncertain, because of the inherent problems in analyzing for Na (see Livi and Veblen, 1987, for details). Despite this problem, the AEM analyses provide valuable compositional information regarding the partitioning of elements

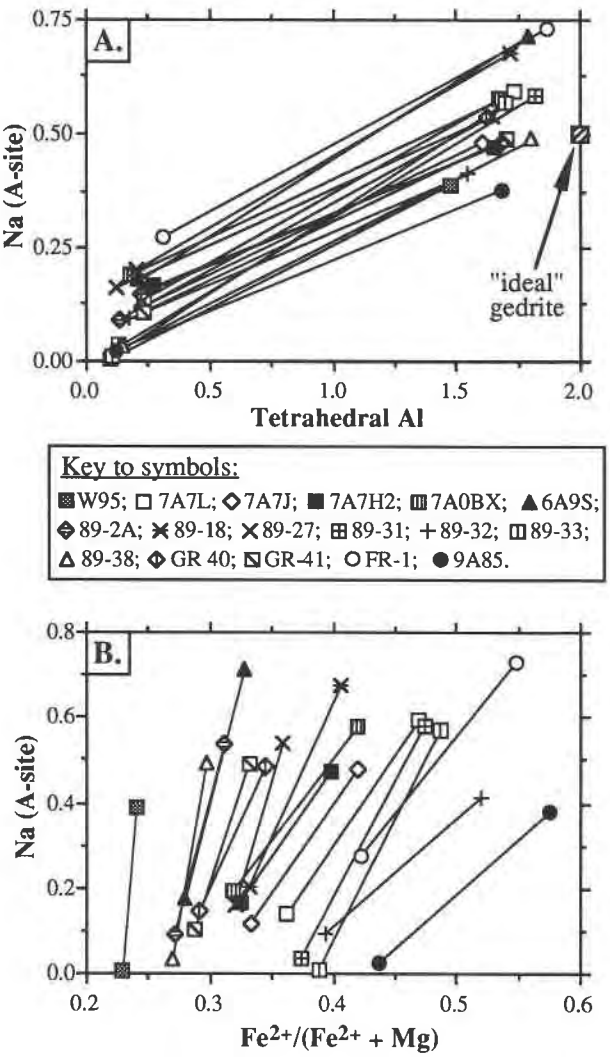


Fig. 18. Average AEM data for exsolved orthoamphibole pairs. (**A**) Plot of calculated A-site occupancy vs. $^{[4]}$Al. The miscibility gap is clearly defined in terms of these site occupancies with the gedrite samples being richer in both A-site occupancy and $^{[4]}$Al. The slopes of the tie lines reflect an $^{[A]}$Na to $^{[4]}$Al ratio from about 0.25 to 0.35. The position for ideal gedrite of Robinson et al. (1971a) is also shown. (**B**) Plot of calculated A-site occupancy vs. $Fe^{2+}/(Fe^{2+} + Mg)$. The previously reported trends of increasing A-site occupancy and a widening of the gap with increased Fe content are not as evident from the AEM data, probably because of the inherent problems in detecting Na in the microscope and the uncertainties in estimating A-site occupancies.

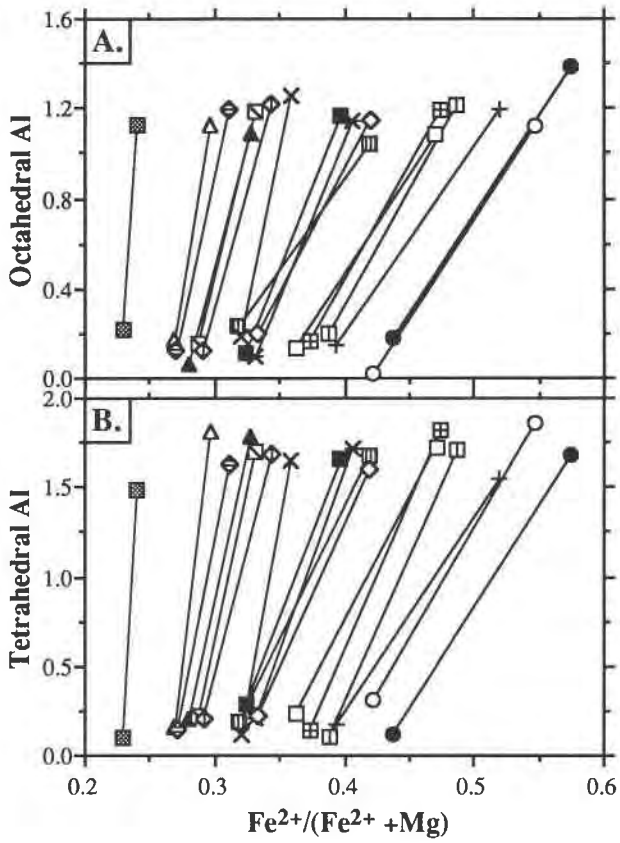


Fig. 19. Average AEM data for exsolved orthoamphibole pairs. (**A**) Octahedral Al vs. $Fe^{2+}/(Fe^{2+} + Mg)$ and (**B**) tetrahedral Al vs. $Fe^{2+}/(Fe^{2+} + Mg)$. Both plots show a slight widening of the gap with increased Fe content. Note for the Fe-rich pairs, the gedrite samples show greater Fe content than coexisting anthophyllite compared with the Mg-rich samples. The Mg-rich gedrite compositions also appear to be slightly depleted in $^{[6]}$Al compared with the Fe-rich samples. Symbols as in Fig. 18.

during exsolution, which cannot be obtained from bulk electron microprobe analyses of submicroscopically exsolved grains.

The miscibility gap between anthophyllite and gedrite can be described by discontinuities primarily in two amphibole substitutions, edenite ($^{[A]}$Na,$^{[4]}$Al $\leftrightarrow$ $^{[A]}\square$,$^{[4]}$Si) and tschermakite ($^{[6]}$Al,$^{[4]}$Al $\leftrightarrow$ $^{[6]}$Mg,$^{[4]}$Si). The work by Robinson et al. (1971a) has emphasized the importance of A-site occupancy (edenite component) in gedrite, and they have proposed an ideal end-member gedrite composition of $Na_{0.5}(Mg,Fe^{2+})_2(Mg,Fe^{2+})_{3.5}Al_{1.5}Si_6Al_2O_{22}(OH)_2$, which is produced by applying the edenite and tschermakite substitutions in a 1:3 ratio to the end-member anthophyllite formula. The results of Spear (1980) have confirmed this trend, but his data indicate that there is considerable deviation from a linear trend between anthophyllite to ideal gedrite caused by the differences in Fe/Mg ratio.

The AEM data obtained in this study on the exsolved phases show element partitioning trends that are in excellent agreement with the results of the above two studies. The AEM data are presented in Figures 18, 19, and 20. For each sample, the anthophyllite and gedrite compositions are average AEM compositions from a number of individual analysis points. In Figure 18, calculated A-site occupancy is plotted vs. $^{[4]}$Al and $Fe^{2+}/(Fe^{2+} + Mg)$. Because all analyses are normalized assuming all Fe as FeO, the cation totals are maximized and the A-site contents may be slightly overestimated.

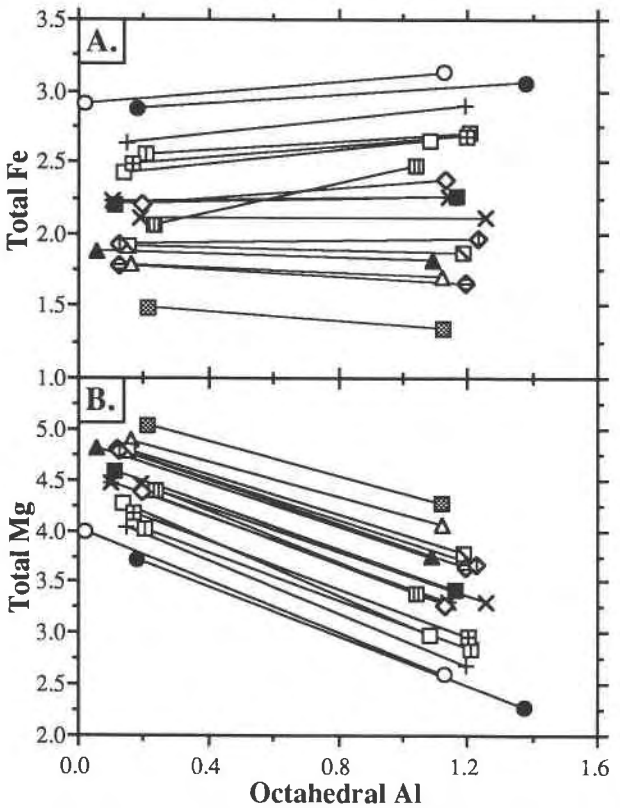


Fig. 20. Average AEM data for exsolved orthoamphibole pairs. (**A**) $Fe_{tot}$ and (**B**) $Mg_{tot}$ vs. $^{[6]}Al$ for all exsolved pairs. Fe concentration remains relatively constant during exsolution with the change in the $Fe^{2+}/(Fe^{2+} + Mg)$ ratio caused by the predominant effect of the $^{[6]}Al,^{[4]}Al \leftrightarrow {}^{[6]}Mg,^{[4]}Si$ exchange. The changing slope of the tie lines in **A** around $Fe_{tot} = 2.25$ may reflect an increasing amount of ferritschermakite exchange, $^{[6]}Fe^{3+},^{[4]}Al \leftrightarrow {}^{[6]}Mg,^{[4]}Si$, in Fe-rich samples. Symbols as in Fig. 18.

The calculated A-site occupancy for the anthophyllite lamellae ranges from 0.0 to 0.27. In coexisting gedrite samples, this range is 0.38–0.73. Values of $^{[4]}Al$ range from 0.03 to 0.31 in anthophyllite and from 1.47 to 1.86 in gedrite. In Figure 18A, the slopes of the tie lines reflect an $^{[A]}Na$ to $^{[4]}Al$ ratio from about 0.25 to 0.35. The wider gap in $^{[4]}Al$ content for the exsolved pairs, compared with the pairs of Spear (1980), is consistent with compositions developed at lower temperatures. The tendency of Fe-rich orthoamphiboles to be enriched in $^{[A]}Na$, shown so well by Spear's data, is not as evident in the AEM analyses (Fig. 18B). The widening of the gap with the increasing $Fe^{2+}/(Fe^{2+} + Mg)$ ratio can be seen in Figure 18B, but it also is not as pronounced as in Spear (1980, his Fig. 5). The scatter, which obscures these trends, is probably due to factors already discussed involving Na detection with AEM and calculating A-site occupancies.

The $^{[6]}Al$ ranges from 0.02 to 0.23 in the anthophyllite and from 1.04 to 1.38 for the gedrite. This gap in $^{[6]}Al$ is also slightly larger than that of Spear (1980), consistent with formation at slightly lower temperatures. The $^{[6]}Al$ and $^{[4]}Al$ contents for the exsolved orthoamphiboles are plotted vs. $Fe^{2+}/(Fe^{2+} + Mg)$ in Figure 19. There is a slight tendency for Mg-rich orthoamphiboles to be depleted in $^{[6]}Al$, which is the opposite of what Spear observed. Moreover, there appears to be a slight, but noticeable, widening of the gap with the increasing $Fe^{2+}/(Fe^{2+} + Mg)$ ratio in terms of $^{[6]}Al$, a pattern not shown by Spear's data. In Figure 19B, the Fe-rich orthoamphiboles tend to show greater differences in $Fe^{2+}/(Fe^{2+} + Mg)$ ratios between exsolved pairs of anthophyllite and gedrite than for Mg-rich compositions. This change from a near-vertical slope of the tie lines in Mg-rich compositions to positive slopes for Fe-rich compositions is also evident in Figure 19A. Figure 20 shows plots of $Fe_{tot}$ and $Mg_{tot}$ vs. $^{[6]}Al$ for the exsolved pairs. Note that there are distinct differences in $Mg_{tot}$ content between coexisting anthophyllite and gedrite while the $Fe_{tot}$ contents remain fairly constant. This observation, also noted by Stout (1971) and Spear (1980), implies that during exsolution the tschermakite substitution predominates over the ferrotschermakite substitution. This result is supported by the single-crystal X-ray refinements of gedrite and anthophyllite by Papike and Ross (1970) and Finger (1970), respectively, showing very low Fe contents in M2.

Careful examination of the tie lines in Figure 20A, however, reveals a definite change in slope from slightly negative to slightly positive, occurring at a $Fe_{tot}$ value of about 2.25. This observation combined with the data in Figure 19 suggest that the ferritschermakite exchange, $^{[6]}Fe^{3+},^{[4]}Al \leftrightarrow {}^{[6]}Mg,^{[4]}Si$, may become more significant for Fe-rich samples. This would result in gedrite having more $Fe_{tot}$ than coexisting anthophyllite, which is consistent with the AEM data. The Mössbauer spectroscopy study of Bancroft et al. (1966) for anthophyllite and the site occupancy refinements of gedrite by Papike and Ross (1970) indicate that larger amounts of $Fe^{2+}$ occur at M2 with increasing Fe/Mg ratio, which might lead to considerable ferrotschermakite exchange, $^{[6]}Al,^{[4]}Al \leftrightarrow {}^{[6]}Fe^{2+},^{[4]}Si$. This would, however, lead to anthophyllite having more Fe than gedrite, a trend not supported by the AEM data. The greater increase in Fe content for gedrite over coexisting anthophyllite can also be explained by the increasing operation of other amphibole substitutions and partitioning of Fe and Mg among M1, M3, and M4 with decreasing temperature, as discussed by Robinson et al. (1971a). The details of the relationships between various site occupancies and composition for orthoamphiboles await additional site-occupancy refinements from single-crystal XRD and spectroscopic studies.

### Comparison with electron microprobe analyses

Many of the samples (or localities) examined in this study have been the subject of previous work on orthoamphiboles and the orthoamphibole solvus (Table 1). In all of the previous work, amphibole compositions were determined either by wet chemical analysis or by electron microprobe (EMP). The analyses of Spear (1980, 1982) show compositions for several pairs of coexisting, dis-

crete grains of anthophyllite and gedrite. In this section we compare the previously reported EMP data with the AEM data for similar samples. The compositional data are compared on a series of $^{[A]}$Na vs. $^{[6]}$Al diagrams (Fig. 21). If the unmixing process in orthoamphiboles involved only the edenite and tschermakite substitutions, then the A-site occupancy would be due to the edenite substitution, and the $^{[6]}$Al would come from the tschermakite substitution. In this case, one would expect the preexsolution amphibole compositions to fall right on the tie line between the exsolved compositions. For some of the data shown in Figure 21, this is nearly the case.

**Amphibole Hill.** Figure 21A–21E shows amphibole compositions from the Amphibole Hill area. Samples from outcrop 6A9 of Robinson et al. (1971a) and 7A7L of Schumacher (personal communication) show compositions near the center of the solvus (Fig. 21A, 21B, respectively). Two samples from outcrop 6A9 were studied with TEM and AEM (6A9S and 89-2). Note that the analyses, 6A9X and 6A9S, plot relatively close to the tie line for 89-2, especially 6A9S. The tie line for exsolved pairs in 6A9S shows a considerable increase in A-site occupancy for both anthophyllite and gedrite. This shifting of tie lines appears in several of the plots and may be due to uncertainties in calculating A-site occupancies. It is also possible that the preexsolution amphibole compositions shown by wet chemical and microprobe analyses do not plot on the tie lines for the exsolved pairs simply because of outcrop-scale compositional heterogeneities in the rocks. Shown at the base of Figure 21A is the AEM pair of Gittos et al. (1976), from sample 6A9X. The position of this pair, compared with the present AEM data, reflects the improved resolution of modern AEM instrumentation and the inability of early instruments to measure Na. Both of these samples (6A9S and 7A7L) show very coarse, pervasive exsolution textures (see Figs. 4 and 8), which are consistent with their being near the center of the solvus. Figure 21C shows results for locality W95. These gneisses, containing enclaves of Al-bearing minerals, have been extensively studied by Robinson and Jaffe (1969b) and Schumacher and Robinson (1987). For analysis W95SX (Schumacher and Robinson, 1987), both the compositions with all Fe as FeO and the normalized compositions (to 15 cations excluding Na and K) are shown. The small amounts of $Fe^{3+}$ produce only a slight decrease in $^{[6]}$Al. Analysis W95JX (given in Robinson et al., 1971a) plots very near the tie line.

Samples 7A0BX (see Schumacher and Robinson, 1986) and 7A7J have much more aluminous bulk compositions. In fact, both these rocks contain gedrite with compositions clearly outside the miscibility gap (Fig. 21D, 21E). Other gedrite samples show bulk compositions that appear to be near the gedrite limb of the solvus, as indicated by their positions relative to the AEM data for the exsolved pairs. The exsolution textures in these samples (Table 2), consisting of small, scattered, heterogeneously nucleated lamellae, some GP zones, and large areas of homogeneous gedrite, also suggest a position near

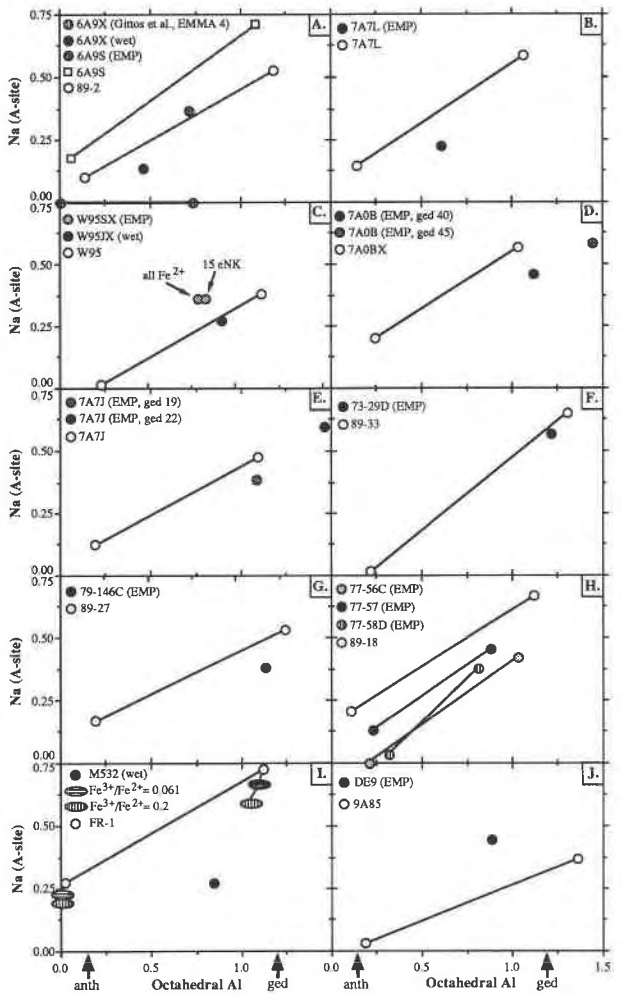


Fig. 21. Comparison of AEM compositions from exsolved pairs of anthophyllite and gedrite with previously reported EMP compositions for similar samples (see Table 1). The miscibility gap is shown in terms of A-site occupancy vs. $^{[6]}$Al. Each plot has its own key to the symbols, giving pertinent sample numbers. Tie lines connect all coexisting pairs. Most of the EMP analyses represent preexsolution amphibole compositions that fall between the exsolved compositions. The exsolved pairs represent the widest miscibility gap so far found in the orthoamphiboles, reflecting lower temperatures of formation farther down on the solvus limbs. Plots (**A**) through (**E**) are for samples from Amphibole Hill (EMMA-4 data in **A** from Gittos et al., 1976); (**F**) through (**H**) are for samples from the Post Pond area; and (**I**) and (**J**) are for samples from Colorado.

or outside the miscibility gap. None of the extremely Al-rich gedrite samples was studied with TEM.

**Post Pond area.** Compositions of orthoamphiboles from east-central Vermont are shown in Figure 21F–21H. These amphibolites often show considerable heterogeneity and may be layered. The samples used in this study were collected at or near mapped outcrops but do not represent the same exact samples discussed by Spear (1980, 1982).

As in the Amphibole Hill samples, the exsolution textures reflect the location along the anthophyllite gedrite

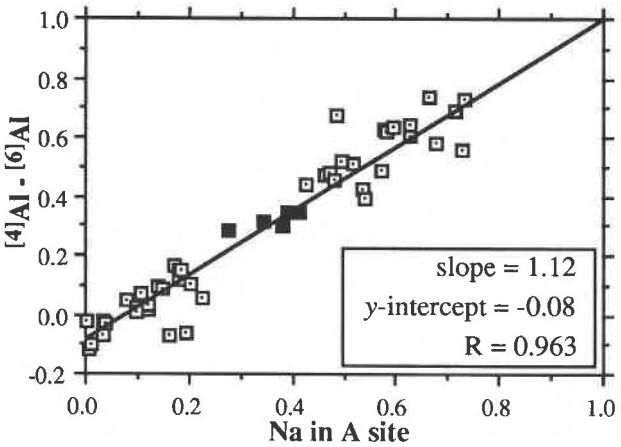


Fig. 22. Plot of calculated A-site occupancy vs. ($^{[4]}$Al-$^{[6]}$Al) for all exsolved pairs of orthoamphiboles (open symbols) and several bulk AEM analyses from exsolved areas (solid symbols). A least-squares fit to this data shows a straight-line fit with a slope of 1.12, a $y$-intercept of $-0.08$, and a correlation coefficient, $R$, of 0.963. This demonstrates the dominant operation of the edenite and tschermakite substitutions during exsolution. The scatter in the data may be due to inaccuracies in determining A-site occupancy or the involvement of other amphibole substitutions.

join of the discrete grain analyses reported by Spear (1980, 1982). Compositions near the limb of the solvus (89-33, Fig. 21F) produce textures consisting of small, homogeneously and heterogeneously nucleated lamellae, with some larger lamellae along (010) CWEs. Analysis 79-146C of Spear (1982) plots a little toward the center of the miscibility gap (89-27, Fig. 21G), and our samples from this locality contain well-developed exsolution textures, composed of large (010) lamellae forming along CWEs, with small homogeneously nucleated precipitates growing between them (see Fig. 12).

Sample 89-18, an anthophyllite-rich rock, was collected in the vicinity of Spear's locality 77-57. Coexisting anthophyllite and gedrite pairs from three of Spear's samples, 77-56C, 77-57, and 77-58D, are plotted for comparison in Figure 21H. All the EMP compositions show lower A-site occupancies, but the slopes of the tie lines are generally in agreement with the exsolved pair. Clearly the exsolved pairs represent compositions farther out on both limbs of the solvus, reflecting lower temperatures compared with the initial crystallization of distinct anthophyllite and gedrite grains in these rocks.

**Colorado samples.** Figure 21I and 21J shows comparisons for the gedrite samples from Colorado. Sample FR-1, from the Front range, was studied by Gable and Sims (1969), who reported the wet chemical analyses for the gedrite sample (analysis M532) plotted in Figure 21I. This preexsolution amphibole composition plots near the middle of the solvus, and the gedrite samples show coarse (010) anthophyllite lamellae (see Fig. 1). The tie line for the exsolved pair is displaced substantially from the bulk analysis, with both anthophyllite and gedrite having high A-site occupancies. These gedrite samples are Fe-rich (Fig. 19), and this discrepancy may be due in part to $Fe^{3+}$ in these samples. For Figure 21I, we have recalculated the AEM analyses assuming $Fe^{3+}/Fe^{2+}$ ratios of 0.061 (Gable and Sims, 1969) and 0.2. The results do shift the tie line down slightly toward the bulk analysis. It could be that the gedrite samples we collected contain slightly more $Na_2O$ than the original samples of Gable and Sims.

For sample 9A85, also an Fe-rich sample from Ohio City, Colorado, the preexsolution analysis (DE9) is from Earley and Stout (1991). The exsolution textures are also relatively coarse in this sample (see Figs. 5 and 6), consistent with the preexsolution composition lying near the center of the solvus.

The relationships presented in Figure 21 are consistent, for the most part, with the edenite and tschermakite substitutions (involving the T, M2, and A sites), being primarily responsible for the exsolution. Another way to verify the primary operation of these two substitutions is to plot $^{[A]}$Na vs. ($^{[4]}$Al-$^{[6]}$Al). If edenite and tschermakite substitutions are solely responsible for A-site occupancy, $^{[4]}$Al, and $^{[6]}$Al, then the analyses should fall along a straight line of slope 1, passing through the origin. Such a plot has been made for the AEM data (Fig. 22), including compositions from exsolved pairs and several broad-beam AEM analyses from exsolved areas. A linear regression analysis of the data reveals a slope of 1.12, a $y$ intercept of $-0.08$, and a correlation factor, $R$, of 0.963. This result emphasizes the dominance of these two amphibole substitutions.

## Discussion

### Exsolution mechanisms

The exsolution microstructures observed in the orthoamphiboles suggest that both heterogeneous and homogeneous nucleation and growth were common processes during exsolution. Evidence for heterogeneous nucleation along (010) CWEs and (100) stacking faults was common in many of the samples (Figs. 9–15, Table 2). The unusual morphologies of the exsolution lamellae (bulging and embayments) in the vicinity of these defects, especially at the defect terminations, are thought to be the result of the structural distortion and associated strain energy, which lead to boundary pinning of the lamellar interfaces and enhanced diffusion along the large structural tunnels created by defect terminations. Heterogeneous nucleation of exsolution lamellae has also been observed at microfractures, amphibole subgrain boundaries, dislocations, and the interfaces of ilmenite and rutile needles in the amphibole. In general, the coarsest observed exsolution lamellae appear to be the result of heterogeneous nucleation, indicating that this was the first unmixing process to begin during slow cooling of many of the amphiboles.

Many samples show evidence of homogeneous nucleation and growth in the form of abundant GP zones or what appear to be intermediate stages of coarsening of GP zones (Figs. 3, 12, 14, 15). Some samples show rela-

tively coarse lamellae that are free of defects and also may have formed by a homogeneous nucleation process (Figs. 1, 4, 7, 8). In most of the amphiboles, evidence for a continual progression of exsolution exists, indicating that both heterogeneous and homogeneous nucleation occurred, perhaps simultaneously (Figs. 12, 15) during slow cooling of the minerals.

Previous TEM studies of exsolved orthoamphiboles by Gittos et al. (1976) and Christie and Olsen (1974) have revealed coarse, coherent, relatively periodic exsolution microstructures. They suggest that the textures may represent a coarsened spinodal decomposition texture. The textures found in samples FR-1, 89-2, 6A9S, and 7A7L (see Figs. 1, 4, and 8) are similar and may also have formed by a spinodal mechanism. Unfortunately no evidence for earlier stages of spinodal decomposition, like the characteristic tweed patterns observed in spinodally decomposed actinolite hornblende (Smelik et al., 1991), have been observed in any of the orthoamphiboles. Therefore the true exsolution mechanisms for coarse textures like those in Figure 4 remain unknown. The same can also be said regarding the distinction between heterogeneous and homogeneous nucleation and growth mechanisms. In general, once an exsolution texture is fully coarsened, determining the role and timing of defects and the true exsolution mechanism becomes more uncertain.

By far the most common orientation for exsolution lamellae is (010). That is because of the large differences in $b$ axial lengths between anthophyllite and gedrite. Lamellae often deviate slightly from strict (010) orientations, especially in the vicinity of planar defects, where there is considerable lattice strain. The two samples from locality 6A9 at Amphibole Hill contain abundant lamellae in a (120) orientation. The change in orientation from (010) to (120) is due to a decrease in $\Delta b$ between anthophyllite and gedrite, accompanied by an increase in $\Delta a$, as predicted by optimal phase boundary calculations (Fig. 17). For the pair used in the calculations (Table 3), the decrease in $\Delta b$ is thought to be mostly due to an increase in Fe at the M2 site. For samples 89-2 and 6A9S, this decrease and resulting lamellar orientation are more likely due to high Ca contents. Between these end-member orientations there exists a range of orientation that ultimately depends upon the actual differences in unit-cell parameters for the two amphiboles, which may vary from grain to grain, or from area to area within grains, depending on local changes in bulk amphibole composition.

### The anthophyllite gedrite solvus

In his paper on coexisting orthoamphiboles from the Post Pond area, Spear (1980) presents a hypothetical $T$-$X$ solvus between anthophyllite and gedrite in terms of A-site occupancy, $^{[4]}$Al, and $^{[6]}$Al. The AEM data for the exsolved orthoamphibole pairs record a wider gap than the data of Spear, consistent with unmixing at lower temperatures. The actual temperature of exsolution, as represented by the medium and coarse lamellae is, of course, unknown. However, by plotting the AEM data on Spear's solvus diagrams, a temperature range for exsolution in these samples can be estimated (Fig. 23). On these diagrams, supersolvus amphiboles from Amphibole Hill (Robinson et al., 1971a; Schumacher and Robinson, 1987;

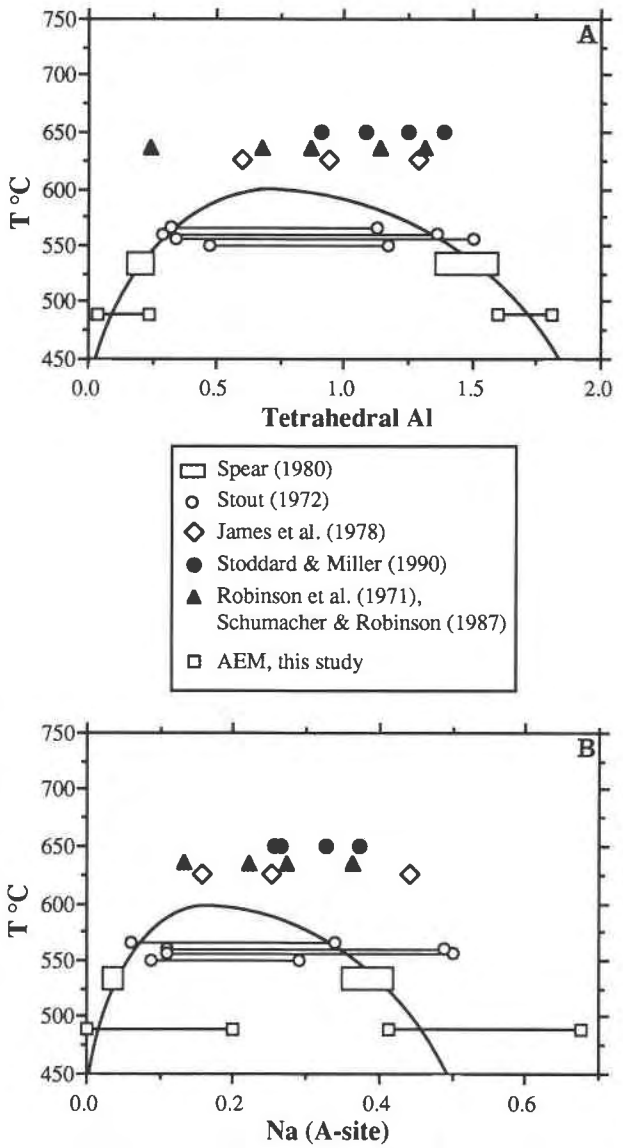


Fig. 23. Hypothetical $T$-$X$ diagrams depicting the orthoamphibole solvus in terms of $^{[4]}$Al (**A**) and A-site occupancy (**B**). These plots are redrawn after Spear (1980), placing the crest of the solvus at 600 (±25) °C, and including the range of exsolved orthoamphibole pairs having $Fe^{2+}/(Fe^{2+} + Mg)$ ratios between 0.3 and 0.5. The EMP data of Spear (1980) and Stout (1972) on coexisting pairs of coarse-grained anthophyllite gedrite are shown, as well as bulk orthoamphibole compositions representing supersolvus conditions from James et al. (1978), Robinson et al. (1971a), Schumacher and Robinson (1987), and Stoddard and Miller (1990). In both diagrams the AEM compositions show a considerably wider gap than previously reported pairs of anthophyllite and gedrite, consistent with the lower temperatures of exsolution. The solvus limbs, as indicated, suggest that the temperature range for exsolution is between about 460 and 520 °C.

Schumacher, personal communication), southeastern California (Stoddard and Miller, 1990), and Ontario (James et al., 1978) are plotted above the crest of the solvus. Coexisting pairs of anthophyllite and gedrite from Stout (1972), which define a narrower gap than Spear's samples, are shown connected by tie lines. The plotting temperatures for the published amphibole compositions are those used by Spear (1980), except for the amphiboles of Stoddard and Miller (1990), which are placed at 650 °C. The range of exsolved anthophyllite and gedrite compositions, determined by AEM, is also shown on these diagrams. The AEM data are plotted at an arbitrary temperature of 490 °C, but they may represent a range of temperature from about 460 to 520 °C. The position of the AEM data is consistent with the solvus limbs of Spear (1980), with the anthophyllite limb steeper than the gedrite limb. In addition, it seems likely that the solubility of gedrite in anthophyllite and vice versa will decrease rapidly at temperatures below about 450 °C, as the amphiboles approach their crystal-chemical limits for $^{[A]}$Na and $^{[4]}$Al. Although the plot for $^{[6]}$Al showed similar trends (not shown), the AEM data suggest that the gedrite limb is much steeper than depicted by Spear (1980).

## Conclusions

A wide range of orthoamphibole samples has been studied with TEM and AEM. The results show that all the amphiboles, even those showing no evidence of exsolution in the petrographic microscope, contain exsolution lamellae. The Al-rich amphiboles do show large regions of homogeneous gedrite but invariably contain some exsolved areas as well. The lamellae range continuously in size from tiny GP zones to platelets up to 200 nm thick, and they show coherent interfaces, except near defect terminations. The lamellae in anthophyllite are usually smaller than those in gedrite (except for the Al-rich gedrite), reflecting the lower solubility of gedrite in anthophyllite. Most samples show evidence for continuous exsolution, with smaller precipitates forming in solute-enriched areas between larger lamellae as cooling progressed. Both homogeneous and heterogeneous nucleation processes occur during exsolution in these samples, and although spinodal decomposition cannot be ruled out altogether, there is no convincing evidence for it in the samples we studied.

Planar defects, including (010) CWEs and (100) stacking faults, are present to varying degrees in all the orthoamphiboles. These defects act as nucleation sites for exsolution and greatly modify the morphologies of the exsolution lamellae. The unusual morphologies are thought to be caused by a combination of lattice strain effects (boundary pinning) and enhanced diffusion associated with the defects.

Lamellar orientations range from (010) to (120), consistent with optimal phase boundary calculations. The exact orientations are strongly dependent on the combined differences in the lengths of the $b$ and $a$ axes of the amphiboles. The Ca content appears to be critical in this regard, leading to decreases in $\Delta b$ and increases in $\Delta a$ between the two amphiboles, resulting in (120) orientations.

The AEM data for exsolved pairs of anthophyllite and gedrite are in agreement with previous EMP analyses for coarse anthophyllite and gedrite pairs, in indicating that the edenite and tschermakite substitutions are the most important during exsolution, and that the gap widens with increased Fe/Mg ratio. The AEM data provide information for the lower temperature regions of the orthoamphibole miscibility gap shown by Spear (1980), and they suggest temperatures of exsolution between 460–520 °C. Additional TEM and AEM examination of orthoamphiboles with extreme Fe/Mg ratios should provide information on the extent of the miscibility gap in Fe-rich regions and perhaps slow closure of the gap in Mg-rich regions.

## Acknowledgments

We would like to express our sincere appreciation to John Schumacher, Dusty Earley, and Jerry Murphy, who provided many of the orthoamphibole samples and unpublished compositional information, without which this study could not have been completed. A special thanks goes to Frank Spear for providing field maps that greatly aided in the collection of the Post Pond samples. Michael Fleet kindly provided the EPLAG program, which is greatly appreciated. We thank Roy Christoffersen and Tami McCormick for their critical reviews of the paper, which clarified several sections. The electron microscopy was undertaken at the transmission electron microscope facility in the Department of Earth and Planetary Sciences at the Johns Hopkins University, supported by NSF grants EAR86-09277 and EAR89-03630, and instrumentation grant EAR83-00365.

## References cited

Bancroft, G.M., Maddock, A.G., Burns, R.G., and Strens, R.G.J. (1966) Cation distribution in anthophyllite from Mössbauer and infra-red spectroscopy. Nature, 212, 913–915.

Bøggild, O.B. (1905) Mineralogia Groenlandica. Meddelelser om Groenland, 32, 400.

——— (1924) On the labradorization of the feldspars. Kongelige Danske Videnskabernes Selskab, Matematisk-Fysisk Meddelelser, 6, 1–79.

Bollman, W., and Nissen, H.-U. (1968) A study of optimal phase boundaries: The case of exsolved feldspars. Acta Crystallographica, A24, 546–557.

Champness, P.E., and Lorimer, G.W. (1976) Exsolution in silicates. In H.-R. Wenk, P.E. Champness, J.M. Christie, J.M. Cowley, A.H. Heuer, G. Thomas, and N.J. Tighe, Eds., Electron microscopy in mineralogy, p. 174–204. Springer-Verlag, Berlin.

Christie, O.H.J., and Olsen, A. (1974) Spinodal precipitation in minerals and some new observations. Bulletin de la Société Français de Minéralogie et de Cristallographie, 97, 202–205.

Coe, R.S., and Kirby, S.H. (1975) The orthoenstatite to clinoenstatite transformation by shearing and reversion by annealing: Mechanism and potential applications. Contributions to Mineralogy and Petrology, 52, 29–55.

Colville, P.A., Ernst, W.G., and Gilbert, M.C. (1966) Relationships between cell parameters and chemical compositions of monoclinic amphiboles. American Mineralogist, 51, 1727–1754.

Crowley, P.D., and Spear, F.S. (1981) The orthoamphibole solvus: $P$, $T$, $X$(Fe-Mg) relations. Geological Society of America Abstracts with Programs, 13, 435.

Earley, D., and Stout, J.H. (1991) Cordierite-cummingtonite facies rocks from the Gold Brick District, Colorado. Journal of Petrology, 32, 1169–1201.

Finger, L.W. (1970) Refinement of the crystal structure of an anthophyllite. Carnegie Institution of Washington Year Book, 68, 283–288.

Fleet, M.E. (1982) Orientation of phase and domain boundaries in crystalline solids. American Mineralogist, 67, 926–936.

——— (1984) Orientation of feldspar intergrowths: Application of lattice misfit theory to cryptoperthites and *e*-plagioclase. Bulletin de Minéralogie, 107, 509–519.

Fleet, M.E., Bilcox, G.A., and Barnett, R.L. (1980) Oriented magnetite inclusions in pyroxenes from the Grenville Province. Canadian Mineralogist, 18, 89–99.

Gable, D.J., and Sims, P.K. (1969) Geology and regional metamorphism of some high grade cordierite gneisses, Front Range, Colorado. Geological Society of America Special Paper, 128, 1–87.

Gittos, M.F., Lorimer, G.W., and Champness, P.E. (1974) An electron-microscopic study of precipitation (exsolution) in an amphibole (the hornblende-grunerite system). Journal of Materials Science, 9, 184–192.

——— (1976) The phase distributions in some exsolved amphiboles. In H.-R. Wenk, P.E. Champness, J.M. Christie, J.M. Cowley, A.H. Heuer, G. Thomas, and N.J. Tighe, Eds., Electron microscopy in mineralogy, p. 238–247. Springer-Verlag, Berlin.

Hawthorne, F.C. (1983) The crystal chemistry of the amphiboles. Canadian Mineralogist, 21, 173–480.

Hawthorne, F.C., Griep, J.L, and Curtis, L. (1980) A three-amphibole assemblage from the Tallan Lake Sill, Peterborough County, Ontario. Canadian Mineralogist, 18, 275–284.

Heinrich, E.W., and Rabbitt, J.C. (1960) Geology of the Cherry Creek area. In Pre-Beltian geology of the Cherry Creek and Ruby Mountains areas, S.W. Montana. Montana Bureau of Mines and Geology Memoir, 38, 114 p.

Iijima, S., and Buseck, P.R. (1975) High resolution electron microscopy of enstatite. I. Twinning, polymorphism, and polytypism. American Mineralogist, 60, 758–770.

——— (1976) High-resolution electron microscopy of unit cell twinning in enstatite. In H.-R. Wenk, P.E. Champness, J.M. Christie, J.M. Cowley, A.H. Heuer, G. Thomas, and N.J. Tighe, Eds., Electron microscopy in mineralogy, p. 319–323. Springer-Verlag, Berlin.

Jaffe, H.W., Robinson, P., Tracy, R.J., and Ross, M. (1975) Orientation of pigeonite exsolution lamellae in metamorphic augite: Correlation with composition and calculated optimal phase boundaries. American Mineralogist, 60, 9–28.

James, R.S., Grieve, R.A.F., and Pauk, L. (1978) The petrology of cordierite-anthophyllite gneisses and associated mafic and pelitic gneisses at Manitouwadge, Ontario. American Journal of Science, 278, 41–63.

Kirby, S.H. (1976) The role of crystal defects in the shear-induced transformation of orthoenstatite to clinoenstatite. In H.-R. Wenk, P.E. Champness, J.M. Christie, J.M. Cowley, A.H. Heuer, G. Thomas, and N.J. Tighe, Eds., Electron microscopy in mineralogy, p. 465–472. Springer-Verlag, Berlin.

Livi, K.J.T., and Veblen, D.R. (1987) "Eastonite" from Easton, Pennsylvania: A mixture of phlogopite and a new form of serpentine. American Mineralogist, 72, 113–125.

——— (1989) Transmission electron microscopy of interfaces and defects in intergrown pyroxenes. American Mineralogist, 74, 1070–1083.

McLaren, A.C., and Etheridge, M.A. (1976) A transmission electron microscope study of naturally deformed orthopyroxenes. Contributions to Mineralogy and Petrology, 57, 163–177.

Papike, J.J., and Ross, M. (1970) Gedrites: Crystal structures and intracrystalline cation distributions. American Mineralogist, 55, 1945–1972.

Robinson, P., and Jaffe, H. (1969a) Chemographic exploration of amphibole assemblages from central Massachusetts and southwestern New Hampshire. Mineralogical Society of America Special Paper, 2, 251–274.

——— (1969b) Aluminous enclaves in gedrite-cordierite gneiss from southwestern New Hampshire. American Journal of Science, 267, 389–421.

Robinson, P., Jaffe, H.W., Klein, C., and Ross, M. (1969) Equilibrium coexistence of three amphiboles. Contributions to Mineralogy and Petrology, 22, 248–258.

Robinson, P., Ross, M., and Jaffe, H. (1970) The composition field of anthophyllite and the anthophyllite miscibility gap. American Mineralogist, 55, 307–309.

——— (1971a) Composition of the anthophyllite-gedrite series, comparisons of gedrite and hornblende, and the anthophyllite-gedrite solvus. American Mineralogist, 56, 1005–1041.

Robinson, P., Jaffe, H.W., Ross, M., and Klein, C. (1971b) Orientations of exsolution lamellae in clinopyroxenes and clinoamphiboles: Consideration of optimal phase boundaries. American Mineralogist, 56, 909–939.

Robinson, P., Ross, M., Nord, G.L., Jr., Smyth, J.R., and Jaffe, H.W. (1977) Exsolution lamellae in augite and pigeonite: Fossil indicators of lattice parameters at high temperature and pressure. American Mineralogist, 62, 857–873.

Robinson, P., Spear, F.S., Schumacher, J.C., Laird, J., Klein, C., Evans, B.W., and Doolan, B.L. (1982) Phase relations of metamorphic amphiboles: Natural occurrence and theory. In Mineralogical Society of America Reviews in Mineralogy, 9B, 1–227.

Ross, M., Papike, J.J., and Shaw, K.W. (1969) Exsolution textures in amphiboles as indicators of subsolidus thermal histories. Mineralogical Society of America Special Paper, 2, 275–299.

Schumacher, J.C. (1988) Stratigraphy and geochemistry of the Ammonoosuc volcanics, central Massachusetts and southwestern New Hampshire. American Journal of Science, 288, 619–663.

Schumacher, J.C., and Robinson, P. (1986) Gedrite-cordierite gneisses and related metamorphosed volcanic rocks, Keene Dome, southwestern New Hampshire. In P. Robinson and D.C. Elbert, Eds., Field trip guidebook: Regional metamorphism and metamorphic phase relations in northwestern and central New England. 14th General Meeting, International Mineralogical Association, Contribution No. 59, p. 145–194. Department of Geology and Geography, University of Massachusetts, Amherst, Massachusetts.

——— (1987) Mineral chemistry and metasomatic growth of aluminous enclaves in gedrite-cordierite-gneiss from southwestern New Hampshire. Journal of Petrology, 28, 1033–1073.

Seifert, F. (1977) Compositional dependence of the hyperfine interaction of $^{57}Fe$ in anthophyllite. Physics and Chemistry of Minerals, 1, 43–52.

Seifert, F., and Virgo, D. (1974) Temperature dependence of intracrystalline $Fe^{2+}$-Mg distribution in a natural anthophyllite. Carnegie Institution of Washington Year Book, 73, 405–411.

——— (1975) Kinetics of the $Fe^{2+}$-Mg order-disorder reaction in anthophyllites: Quantitative cooling rates. Science, 188, 1107–1109.

Smelik, E.A., and Veblen, D.R. (1991) Exsolution of cummingtonite from glaucophane: A new orientation for exsolution lamellae in clinoamphiboles. American Mineralogist, 76, 971–984.

Smelik, E.A., Nyman, M.W., and Veblen, D.R. (1991) Pervasive exsolution within the calcic amphibole series: TEM evidence for a miscibility gap between actinolite and hornblende in natural samples. American Mineralogist, 76, 1184–1204.

Spear, F.S. (1977) Phase equilibria of amphiboles from the Post Pond volcanics, Vermont. Carnegie Institution of Washington Year Book, 76, 613–619.

——— (1978) Petrogenetic grid for amphibolites from the Post Pond and Ammonoosuc volcanics. Carnegie Institution of Washington Year Book, 77, 805–808.

——— (1980) The gedrite-anthophyllite solvus and the composition limits of orthoamphibole from the Post Pond Volcanics, Vermont. American Mineralogist, 65, 1103–1118.

——— (1982) Phase equilibria of amphibolites from the Post Pond Volcanics, Mt. Cube Quadrangle, Vermont. Journal of Petrology, 23, 383–426.

Spear, F.S., and Rumble, D. (1986a) Pressure, temperature, and structural evolution of the Orfordville Belt, west-central New Hampshire. Journal of Petrology, 27, 1071–1093.

——— (1986b) Mineralogy, petrology and *P-T* evolution of the Orfordville area, west-central New Hampshire and east-central Vermont. In P. Robinson, and D.C. Elbert, Eds., Field trip guidebook: Regional metamorphism and metamorphic phase relations in northwestern and central New England. 14th General Meeting, International Mineralogical Association, Contribution No. 59, p. 57–93. Department of Geology and Geography, University of Massachusetts, Amherst, Massachusetts.

Stoddard, E.F., and Miller, C.F. (1990) Chemistry and phase petrology of amphiboles and orthoamphibole-cordierite rocks, Old Woman Mountains, SE California, USA. Mineralogical Magazine, 54, 393–406.

Stout, J.H. (1970) Three-amphibole assemblages and their bearing on the anthophyllite-gedrite miscibility gap (abs.). American Mineralogist, 55, 312–313.

——— (1971) Four coexisting amphiboles from Telemark, Norway. American Mineralogist, 56, 212–224.

——— (1972) Phase petrology and mineral chemistry of coexisting amphiboles from Telemark, Norway. Journal of Petrology, 13, 99–146.

Treloar, P.J., and Putnis, A. (1982) Chemistry and microstructure of orthoamphiboles from cordierite-amphibole rocks at Outokumpu, North Karelia, Finland. Mineralogical Magazine, 45, 55–62.

Veblen, D.R. (1991) Polysomatism and polysomatic series: A review and applications. American Mineralogist, 76, 801–826.

Veblen, D.R., and Buseck, P.R. (1979) Chain-width order and disorder in biopyriboles. American Mineralogist, 64, 687–700.

——— (1980) Microstructures and reaction mechanisms in biopyriboles. American Mineralogist, 65, 599–623.

Wolter, H.U., and Seifert, F. (1984) Mineralogy and genesis of cordierite-anthophyllite rocks from the sulfide deposit of Falun, Sweden. Lithos, 17, 147–152.

Manuscript received November 8, 1991
Manuscript accepted January 19, 1993